NIAC Phase I Final Report: On-Orbit, Collision-Free Mapping of Small Orbital Debris

PI: Christine Hartzell *

Co-I: Dave Akin

Graduate Students: Alexis Truitt and Jackson Shannon

Undergraduate Students: Benjamin Quock, Nick Behnke, Jooneon Kim and Gregorio Zimmerman

06/30/2019

Abstract

Sub-centimeter orbital debris is currently undetectable using ground-based radar and optical methods. However, the pits in Space Shuttle windows produced by paint chips (e.g. the 3.8mm diameter pit produced by a 0.2mm paint chip on STS-7 [1]) demonstrate that small debris can cause serious damage to spacecraft. Recent analytical, computational and experimental work [2, 3, 4] has shown that charged objects moving quickly through a plasma will cause the formation of solitons in the plasma density. Due to their exposure to the solar wind plasma environment, even the smallest space debris will be charged. Depending on the debris size, charge and velocity, the plasma signature of the solitons may be detected by simple instrumentation on spacecraft. We will describe the amplitude and velocity of solitons that may be produced by mm-cm scale orbital debris in LEO. We will discuss the feasibility of mapping sub-cm orbital debris using a fleet of CubeSats equipped with Langmuir probes. The time and fleet size required to map the debris will also be described. Plasma soliton detection would be the first collision-free method of mapping the small debris population.

Contents

1 Introduction **2**

2 Plasma Soliton Characteristics **4**

2.1 The Plasma Environment 4
2.2 Solitons 4
2.3 Plasma Fluid Equations 6
2.3.1 Derived Coefficients 8
2.3.2 Derived Force 9
2.3.3 Numerical Methods 10
2.4 Code Validation 12
2.5 Orbital Debris Simulation Results 16
2.5.1 Low LEO 18
2.5.2 High LEO Region 1 19
2.5.3 High LEO Region 2 19

*hartzell@umd.edu, Department of Aerospace Engineering, University of Maryland

2.5.4 Polar LEO . . . 20
2.5.5 GEO . . . 21
2.6 Discussion . . . 22
2.7 Summary . . . 24

3 CubeSat Constellation Orbit Design 25
3.1 Methods . . . 25
3.2 Orbit Simulation Results . . . 26
3.3 Discussion . . . 27
3.4 Summary . . . 28

4 CubeSat Design 29
4.1 Communications . . . 29
4.1.1 Radio Frequency Selection . . . 29
4.1.2 Radio Transceiver Selection . . . 30
4.1.3 Antenna Selection . . . 30
4.2 Command and Data Handling System . . . 31
4.3 Attitude Determination and Control System . . . 31
4.4 Electrical Power System . . . 32
4.4.1 Design and Components . . . 32
4.5 Thermal System . . . 33
4.6 Structures . . . 33
4.6.1 Deployable Booms . . . 34
4.7 End of Life Disposal . . . 35
4.8 6U Form Factor . . . 36
4.9 Summary . . . 37

5 Soliton Detection 37
5.1 Langmuir Probe Design . . . 37
5.1.1 Langmuir Probe Theory . . . 37
5.1.2 Instrument Geometry . . . 38
5.1.3 CubeSat Mounting . . . 39
5.1.4 Power Requirements . . . 40
5.2 Probe Operations . . . 40
5.3 Limitations of Langmuir Probes . . . 40
5.3.1 CubeSat Surface Charging . . . 40
5.3.2 Contamination Effects . . . 41
5.4 Data Volume . . . 41
5.5 Summary . . . 41

6 Alternate Architectures 42
6.1 Ground Based Detection of Solitons . . . 42
6.2 Hosted Payload . . . 42

7 Conclusions and Future Directions 43

1 Introduction

According to NASA's Orbital Debris Program Office, it is currently estimated that there are more than 100 million pieces of orbital debris smaller than 1 centimeter in orbit [5]. Small orbital debris can be created during nominal operations (e.g., paint chips, zip ties, errant bolts and nuts) or during catastrophic events, such as spacecraft collisions or explosions. However, due to high orbital velocities, even very small orbital debris can pose a significant risk to spacecraft. For example, a 3.8mm diameter pit was produced in a Space Shuttle window by a 0.2mm paint chip on STS-7 [1]. This small debris can also degrade solar panel output

and damage mission-critical electronics. Furthermore, a 1cm aluminum sphere is predicted to remain in orbit for years (if released 600km altitude), or even centuries (if released at 1000km altitude) [6]. However, small orbital debris cannot be detected using traditional methods. NASA's orbital debris detection program currently relies on radar (through the Haystack and Goldstone facilities) and optical observations (by the Meter Class Autonomous Telescope) [7]. These terrestrial observations are very limited for small debris: the 2015 NASA Technology roadmap identifies "a critical data gap for debris between 0.5 and 3 millimeter in LEO," [7]. In order to estimate the population statistics for small debris, NASA has relied on post-flight analysis of the impact craters on spacecraft exposed to the orbital environment (see [8] for a full description). The most systematic investigation of small orbital debris was the Long Duration Exposure Facility (LDEF); a spacecraft covered in material coupons specifically designed to record the response of these materials to the space environment during its six year mission. Collision-based detection methods have significant drawbacks: 1. collision based-methods only capture the population statistics in a small altitude region (e.g., the LDEF was only able to detect debris in the 330-480km altitude range [8]) and 2. collision based-methods cannot characterize how the debris environment may be changing in time. It is necessary to understand the debris environment in a wide range of altitudes in order to identify regions of increased risk to spacecraft. Additionally, understanding the time-varying plasma environment will be critical to evaluate the efficacy of future remediation efforts. Thus, given the hazard posed by small debris, it is necessary to develop new methods to map the time- and altitude-varying sub-cm debris environment.

Solitons are wave structures similar to standing waves that can occur in a variety of media when nonlinear and dispersive forces are balanced. Solitons were first observed in observed traveling ahead of a boat in a channel in 1834 [9]. Solitons are commonly studied in fluid systems and have been observed in Earth's atmosphere [10]. Solitons have been previously detected in plasma at Earth's magnetopause [11].

Sen and coworkers [2, 3, 4] have recently shown analytically, computationally and experimentally that solitons can be produced in the plasma density by charged objects moving at Mach speeds of approximately 0.5-1.5 (as compared to the ion acoustic velocity) through a plasma. Sen and coworkers have shown that the effect of a charged object moving through a plasma can be described by the forced Korteweg de Vries (fKdV) equation, a partial differential equation which is most frequently studied in fluid mechanics. Note that all orbital debris is electrically charged due to its interaction with the solar wind plasma and the solar UV radiation (which can cause photoemission). There are several solutions to the fKdV equation, including precursor solitons that travel ahead of the charged object at velocities faster than the charged object itself [2]. Thus, Sen [2] predicted that cm-scale LEO orbital debris would produce electric field perturbations of mV/cm that, if detected, could warn of the subsequent arrival of a debris object.

Sen's work focused on the fundamental properties of plasma solitons. In this work, we will investigate the specific properties of solitons produced by orbital debris. Specifically, we will numerically simulate the solitons produced by debris of varying size and electrical charge at varying plasma densities (which correspond to different altitudes) in order to predict the amplitude, velocity, and frequency of production of the resulting solitons. These simulations indicate the range of altitudes at which debris of a given size would be expected to produce solitons as well as the size of debris that would produce solitons. These predictions are critical to evaluating the feasibility of mapping sub-cm orbital debris by detecting their plasma soliton signals.

The precursor solitons manifest in plasma density and, consequently, electric field signatures. The electric potential of a plasma is often measured using Langmuir probes and the electric field and plasma densities can be calculated from the potential measurement. Thus, if of sufficient magnitude, the precursor plasma solitons discovered by Sen *et al.* may be detectable with simple Langmuir probes, which have previously been hosted on CubeSats [12]. We will present a preliminary design of a CubeSat that would detect solitons using Langmuir probes and discuss the limitations of this detection technique. Additionally, we have also simulated the time required to map debris in a 100km altitude range as a function of the speed of soliton dissipation (which dictates how close the CubeSat must be to the debris object) and CubeSat fleet size. The soliton simulations and mission concept presented provide key input in assessing the feasibility of using plasma soliton to detect debris that is currently unobservable, but hazardous to spacecraft.

2 Plasma Soliton Characteristics

Orbital debris becomes charged due to its interaction with the solar wind plasma and the solar UV radiation [13]. It has been theorized that charged orbital debris will cause perturbations in the ion density in the ionospheric plasma, creating ion acoustic solitary waves (IASWs, or solitons) [2]. Sen *et al.* [2, 3, 4] investigated the properties of plasma solitons generally, and did not specifically investigate the feasibility of soliton generation by small orbital debris. We build on Sen *et al.*'s work by simulating the solitons generated using relevant ionospheric plasma and debris properties, with a special emphasis on precursor solitons, which advance upstream of the debris. We seek to determine the debris size and velocity that will produce solitons, as well as the altitude range at where solitons can be produced.

2.1 The Plasma Environment

The ionospheric plasma varies with altitude, latitude and illumination. Low earth orbit (LEO, 200-1000 km altitude) lies within the ionosphere's F2 region. The mid-latitudes of the F2 region consist of low energy, high density plasma (see Table 1), and the dominant ion species is oxygen. Above the F2 layer, between 1000-2000 km altitude, the number of oxygen ions decreases and lighter ions such as hydrogen and helium become dominant. The plasma surrounding geostationary orbits is also high energy and low density, similar to the high latitude LEO regions. Nominal plasma properties for the mid-latitude regions are listed in Table 1 and were derived from various ground-based and space-based observations in [14, 15, 16, 17, 18, 19]. Note that n_e is the electron density, T_e is the electron temperature, m_i is the ion mass, $m_p = 1.67\text{x}10^{-27}$ kg is the proton mass, λ_D is the plasma Debye length, V_d is the velocity of debris in a circular orbit, and V_{ia} is the ion acoustic velocity. For GEO, the dominant ion could be oxygen or hydrogen depending on solar activity, so m_i and V_{ia} are listed for both species.

Table 1: Plasma properties in the mid-latitude ionosphere, derived from ground-based and space-based observations. n_e is the electron density, T_e is the electron temperature, m_i is the ion mass, $m_p = 1.67\text{x}10^{-27}$ kg is the proton mass, λ_D is the plasma Debye length, V_d is the velocity of debris in a circular orbit, and V_{ia} is the ion acoustic velocity. For GEO, the dominant ion could be oxygen or hydrogen depending on solar activity, so m_i and V_{ia} are listed for both species. The table has four columns (ionosphere regions) and nine rows (region and plasma characteristics).

	Low LEO [14]	High LEO 1 [15, 16, 17]	High LEO 2 [15, 16, 17]	GEO [18, 19]
Altitude (km)	700	1200	1400	35,786
Latitude (deg)	0-55	0-55	0-55	0-90
n_e (cm^{-3})	$2\text{x}10^5$	10^5	10^4	1
T_e (eV)	0.25	0.35	0.35	1,000
Ion Species	O^+	H^+	H^+	O^+ / H^+
m_i (m_p)	16	1	1	16 / 1
λ_D (cm)	0.83	1.38	4.36	23,504.00
V_d (km/s)	7.51	7.26	7.16	3.08
V_{ia} (km/s)	1.22	5.75	5.75	77.43 / 309.73

The high latitude, or polar, regions of LEO contain open magnetic field lines, allowing for the escape of particles as well as the entry of high energy particles from the solar wind. The combination of these processes, in addition to geomagnetic storms, creates a highly variable environment [20, 21]. Examples of the plasma environment at high latitudes are provided in Table 2. In general, the plasma density is 10-100x less than the density at mid-latitude regions, with areas of precipitating high energy electrons from the solar wind [20, 21].

2.2 Solitons

Soliton solutions can be derived for many mathematical and physical systems that are modeled by weakly nonlinear partial differential equations, and are caused when the nonlinear and dispersive forces are balanced.

Table 2: Plasma properties in high-latitude ionosphere [20, 21]. For Polar LEO 1, the dominant ion could be oxygen or hydrogen depending on solar activity, so m_i and V_{ia} are listed for both species. The table has three columns (ionosphere regions) and nine rows (region and plasma characteristics).

	Polar LEO 1	Polar LEO 2	Polar LEO 3
Altitude (km)	600	600	950
Latitude (deg)	55-90	55-90	55-90
n_e (cm^{-3})	10	10^4	10^3
T_e (eV)	1,000	0.25	0.35
Ion Species	O^+ / H^+	O^+	H^+
m_i (m_p)	16 / 1	16	1
λ_D (cm)	7,432.00	3.72	13.91
V_d (km/s)	7.56	7.56	7.38
V_{ia} (km/s)	77.43 / 309.73	1.22	5.75

In the partial differential equation shown in Eqn 1, U(x,t) is the wave solution, $\frac{\partial U}{\partial t}$ is the change of the wave over time, $U\frac{\partial U}{\partial x}$ is the nonlinearity of the wave in the x domain, and $\frac{\partial^3 U}{\partial x^3}$ is the dispersion of the wave in the x domain.

$$\frac{\partial U}{\partial t} + U\frac{\partial U}{\partial x} + \frac{\partial^3 U}{\partial x^3} = 0 \tag{1}$$

Solitons are solitary waves that preserve their velocity and shape during translation, assuming transmission through a uniform, constant medium. Solitons remain unaltered if colliding with other solitons. The product of a soliton's amplitude with the square of its width remains constant, and solitons are generated at predictable intervals depending on the amplitude of the source. Solitons can be found throughout nature in a variety of media, to include shallow water, the atmosphere, and plasma [22, 23, 24, 10, 25, 26, 27].

The first recorded solitary wave was observed by John Scott Russell in 1834, who observed a solitary wave in the Union Canal in Scotland. He then reproduced a soliton in a lab experiment using a wave tank, and described the phenomenon in an 1844 publication. Russell described the wave in the Union Canal as follows: "I was observing the motion of a boat which was rapidly drawn along a narrow channel by a pair of horses, when the boat suddenly stopped – not so the mass of water in the channel which it had put in motion; it accumulated round the prow of the vessel in a state of violent agitation, then suddenly leaving it behind, rolled forward with great velocity, assuming the form of a large solitary elevation, a rounded, smooth and well-defined heap of water, which continued its course along the channel apparently without change of form or diminution of speed. I followed it on horseback, and overtook it still rolling on at a rate of some eight or nine miles an hour, preserving its original figure some thirty feet long and a foot to a foot and a half in height." [28] In 1895, Diederick Korteweg and Gustav de Vries derived a nonlinear partial differential equation to describe Russell's soliton experiment, now known as the Korteweg–de Vries (KdV) Equation [29]:

$$\frac{\partial U}{\partial t} + U\frac{\partial U}{\partial x} + \frac{\partial^3 U}{\partial x^3} = 0 \tag{2}$$

More recently, oceanic solitons have been observed with satellite-based synthetic aperture radar [10, 26, 27]. These oceanic surface solitons can be thought of as analogs of solitons generated by orbital debris. Historically, oceanic solitons were described as bands of choppy water or ripplings in the presence of local bathymetry, observed even in calm weather at well known locations. These solitons are often generated when a current of shallow water flows over a submerged obstacle. The solitons propagate radially outward from the obstacle, forming semicircular rings of solitary waves. The height, width, and speed of the solitons, as well as the extent of the semicircular arc, depend on the speed of the current, depth of the water, and the size and shape of the obstacle.

While many variations of the KdV equation have been studied, we will focus on the forced KdV (fKdV) equation, where the solitons are generated due to the presence of a forcing term, $f(x,t)$, as shown in Eqn 3.

In oceanic solitons, the submerged obstacle acts as the force term. Analogously, in the ionosphere, the charged debris is represented as the forcing term.

$$\frac{\partial U}{\partial t} + U\frac{\partial U}{\partial x} + \frac{\partial^3 U}{\partial x^3} = f(x,t) \tag{3}$$

While plasma solitons resulting from charged orbital debris have not yet been detected, the existence of ion acoustic solitons in unmagnetized plasma due to other disturbances has already been demonstrated [25]. Solitons have also previously been observed in the 3D plasma environment of the ionosphere. The Freja scientific satellite observed nonlinear density waves in the upper ionosphere [23], and simulations were conducted to support the observations [24]. Solitons were also observed by the Cluster II satellites at the Earth's magnetopause, created due to turbulence at the boundary [11]. In addition to their theoretical results [2], Sen *et al.* have successfully created solitons in a dusty plasma laboratory experiment [3]. Thus, solitons have been observed experimentally in a variety of applications, including fully 3D systems and space plasmas.

2.3 Plasma Fluid Equations

In the LEO plasma environment, we can assume that the ions are cold relative to the electrons, and the electrons carry all of the current in a Maxwellian distribution. Thus, we can model the equations of state in the plasma using a fluid model. The fluid equations can be derived mathematically by taking moments of the Boltzmann equation. These moments are the standard plasma fluid equations for continuity, momentum, and Poisson's equation, and are used to derive the ion acoustic wave behavior:

$$\frac{\partial n}{\partial t} + \frac{\partial (nu)}{\partial x} = 0 \tag{4}$$

$$\frac{\partial u}{\partial t} + u\frac{\partial u}{\partial x} + \frac{\partial \phi}{\partial x} = 0 \tag{5}$$

$$\frac{\partial^2 \phi}{\partial x^2} - e^{\phi} + n = f(x,t) \tag{6}$$

where n is the ion density, u is the ion velocity, ϕ is the electrostatic potential, and $f(x,t)$ is a forcing function described as a charge density source [2].

We normalize the domain as follows:

$$n = \frac{n}{n_0}, \quad x = \frac{x}{\lambda_D}, \quad t = \frac{V_{ia}}{\lambda_D}t, \quad u = \frac{u}{V_{ia}}, \quad \phi = \frac{e\phi}{k_b T_e} \tag{7}$$

where n_0 is the initial ion density, λ_D is the Debye length, $V_{ia} = \sqrt{k_B T_e / m_i}$ is the ion acoustic velocity, k_B is the Boltzmann constant, m_i is the ion mass, and T_e is the electron temperature.

Assuming a collisionless Maxwellian plasma, the ions are cold relative to the electrons. In the weakly nonlinear limit, we invoke the long wave assumption that the amplitude of the wave is much smaller than the length of the wave. In this weakly nonlinear limit, the plasma fluid equations can be approximated by the KdV Equation, derived by linearizing the plasma fluid equations using the reductive perturbation technique [30]. In this case, with the presence of a forcing term, the plasma fluid equations will be approximated by the forced KdV Equation.

To conduct the perturbation analysis, we create stretched variables, ξ and τ, for the independent variables, x and t:

$$\xi = \epsilon^{1/2}(x - vt) \tag{8}$$

$$\tau = \epsilon^{3/2}t \tag{9}$$

$$\frac{\partial}{\partial x} = \epsilon^{1/2}\frac{\partial}{\partial \xi} \tag{10}$$

$$\frac{\partial}{\partial t} = \epsilon^{1/2} v \frac{\partial}{\partial \xi} + \epsilon^{3/2} v \frac{\partial}{\partial \tau} \tag{11}$$

We then expand the n, u, and ϕ around the unperturbed states in powers of ϵ, where ϵ is a small parameter that measures the weakness of dispersion.

$$n = 1 + \epsilon n_1 + \epsilon^2 n_2 + ... \tag{12}$$

$$u = 0 + \epsilon u_1 + \epsilon^2 u_2 + ... \tag{13}$$

$$\phi = 0 + \epsilon \phi_1 + \epsilon^2 \phi_2 + ... \tag{14}$$

$$f(x,t) = \epsilon^2 f(\xi, \tau) + ... \tag{15}$$

Next, we substitute Eqn 8-Eqn 15 into Eqn 4-Eqn 6. The perturbed continuity equation becomes:

$$\Big(\epsilon^{1/2} v \frac{\partial}{\partial \xi} + \epsilon^{3/2} v \frac{\partial}{\partial \tau}\Big)\Big(1 + \epsilon n_1 + \epsilon^2 n_2\Big) + \Big(\epsilon^{1/2} \frac{\partial}{\partial \xi}\Big)\Big(\Big(1 + \epsilon n_1 + \epsilon^2 n_2\Big)\Big(\epsilon u_1 + \epsilon^2 u_2\Big)\Big) = 0 \tag{16}$$

The perturbed momentum equation becomes:

$$\begin{aligned}\Big(\epsilon^{1/2} v \frac{\partial}{\partial \xi} + \epsilon^{3/2} v \frac{\partial}{\partial \tau}\Big)\Big(\epsilon u_1 + \epsilon^2 u_2\Big) + \Big(\epsilon u_1 + \epsilon^2 u_2\Big)\Big(\epsilon^{1/2} \frac{\partial}{\partial \xi}\Big)\Big(\epsilon u_1 + \epsilon^2 u_2\Big) \\ + \Big(\epsilon^{1/2} \frac{\partial}{\partial \xi}\Big)\Big(\epsilon \phi_1 + \epsilon^2 \phi_2\Big) = 0\end{aligned} \tag{17}$$

The perturbed Poisson equation, using a Taylor expansion of $e^{\phi} \approx 1 + \phi + \frac{\phi^2}{2}$ becomes:

$$\begin{aligned}\Big(\epsilon^{1/2} \frac{\partial}{\partial \xi}\Big)^2 \Big(\epsilon \phi_1 + \epsilon^2 \phi_2\Big) - \Big(1 + \Big(\epsilon \phi_1 + \epsilon^2 \phi_2\Big) + \frac{1}{2}\Big(\epsilon \phi_1 + \epsilon^2 \phi_2\Big)^2\Big) \\ + \Big(1 + \epsilon n_1 + \epsilon^2 n_2\Big) = \epsilon^2 f(\xi, \tau)\end{aligned} \tag{18}$$

After comparing the coefficients of different powers of ϵ, and performing substitution in the set of resulting equations, we arrive at the forced Korteweg–de Vries (fKdV) Equation:

$$\frac{\partial \phi}{\partial \tau} + \phi \frac{\partial \phi}{\partial \xi} + \frac{1}{2} \frac{\partial^3 \phi}{\partial \xi^3} = \frac{1}{2} \frac{\partial f}{\partial \xi} \tag{19}$$

Understanding that fluctuations in the electrostatic potential, ϕ, will drive the nonlinear wave, U, we rewrite the equation using the traditional wave equation form and compare to the fKdV equation often seen in literature:

$$\frac{\partial U}{\partial \tau} + \mu \frac{\partial U}{\partial \xi} + \alpha U \frac{\partial U}{\partial \xi} + \beta \frac{\partial^3 U}{\partial \xi^3} = \frac{1}{2} \frac{\partial f}{\partial \xi} \tag{20}$$

In Eqn 20, U(ξ,τ) is the derived ion acoustic wave, manifested as an electric potential in the plasma surrounding the debris and a perturbation in the ion density. The spatial and temporal variables, ξ and τ, are the derived stretched coordinates of the initial boundary-value problem.

The coefficients α and β define the weighting of the steepening and dispersion terms, and μ is the speed of the medium flowing over the submerged obstacle. Note that in our derivation of Eqn 19 for LEO plasma, $\alpha = 1$, $\beta = 1/2$, and $\mu = 0$ since our reference frame assumes that the medium is static and the submerged obstacle is in motion. The coefficients are discussed in further detail in Section 2.3.1.

Thus, the forced KdV equation has been derived from first principles to describe perturbations in the ion density as a result of charged debris, with the following assumptions: (a) a cold Maxwellian plasma ($T_i < T_e$), (b) a collisionless plasma, meaning that the dust density is negligible ($n_{dust} << n_{ions}$), (c) a weakly nonlinear system, where the amplitude of the wave is much smaller than the length of the wave, and (d) magnetic field effects are negligible and wave propagation can be described in a 1D system, further discussed in Section 2.3.1.

The forced KdV equation will be used in the remainder of this study. In the absence of a forcing term, Eqn 20 reduces to the standard unforced KdV equation in Eqn 21, which is often used in unforced, weakly nonlinear wave studies.

$$\frac{\partial U}{\partial \tau} + \alpha U \frac{\partial U}{\partial \xi} + \beta \frac{\partial^3 U}{\partial \xi^3} = 0 \tag{21}$$

While many studies detail the application of the unforced KdV equation for a variety of fluid systems, there are only a few that discuss application of the forced KdV equation. The works that discuss the generation of IASWs by orbital debris use the fully nonlinear plasma fluid equations instead of the fKdV [2, 3, 4]. Based on the properties of plasma in LEO, we estimate that the amplitude is much smaller than the length of the waves, validating the long wave assumption and allowing for use of the fKdV equation to characterize the solitons. Detailed derivations of the fKdV equation can be found in [31, 32].

2.3.1 Derived Coefficients

Traditionally, the coefficients α and β, when applied to shallow water waves, describe the geometry of the water channel with respect to the flow of the medium and height of the obstacle at the floor of the channel [31, 32]. In our derivation of Eqn 19 for LEO plasma, assuming a collisionless Maxwellian plasma, $\alpha = 1$ and $\beta = 1/2$. We verify these coefficients through study of the derived coefficients for other plasma environments.

For IASWs, these coefficients have been derived in literature for complex plasmas consisting of strong magnetic fields, dust, and superthermal electrons with $\kappa-$distributions using a damped KdV (dKdV) equation as shown in Eqn 22, where γ is the coefficient for the additional damping term due to ion-neutral collisions [33, 34, 35, 36].

$$\frac{\partial U}{\partial \tau} + \alpha U \frac{\partial U}{\partial \xi} + \beta \frac{\partial^3 U}{\partial \xi^3} + \gamma U = 0 \tag{22}$$

It can be shown that for a cold plasma with negligible dust density and a weak magnetic field, the complex plasma coefficients reduce to [33, 34]:

$$\alpha = \frac{3a_\kappa(1/\rho^{1/2}) - 2b_\kappa(\rho^{1/2}/z_i)}{2a_\kappa^{3/2}} \tag{23}$$

$$\gamma = \frac{\vartheta}{2} \tag{24}$$

$$\beta = \frac{\rho^{1/2}}{2a_\kappa^{3/2}} \tag{25}$$

where

$$a_\kappa = \frac{2\kappa - 1}{2\kappa - 3} \qquad b_\kappa = \frac{4\kappa^2 - 1}{2(2\kappa - 3)^2} \tag{26}$$

$$\rho = \frac{z_i^2 n_{0i}}{n_{0e}} \qquad \vartheta = \frac{\omega_{Bi}}{\omega pi} << 1 \tag{27}$$

Here, n_{0i} and n_{0e} are the unperturbed ion and electron densities, z_i is the ion charge state, ϑ is the ion-neutral collision frequency, ω_{Bi} is the ion cyclotron frequency, and ω_{pi} is the ion plasma frequency. Assuming a Maxwellian plasma ($\kappa \to \infty$) for the plasma regions in Table 1 and Table 2, the coefficients using Eqn 23 - Eqn 27 are again calculated as $\alpha = 1$, $\beta = 1/2$, and $\gamma = 0$, agreeing with our derivation of Eqn 19. It is important to note that these coefficients are simplified since we have assumed a collisionless Maxwellian plasma, with negligible dust density and the magnetic field effects. However, the velocity distribution function of space plasmas typically have a suprathermal tail and are modeled with kappa distribution functions instead of a Maxwellian model [37, 38]. Considering the estimated kappa value from recent Earth magnetospheric models ($\kappa = 100$) [39, 40], the coefficients become:

$$\alpha = 1.0051 \qquad \beta = 0.4925 \qquad \gamma = 0 \tag{28}$$

We will use the $\kappa-$distribution coefficients in Eqn 28 for the remainder of this investigation.

One must consider the dispersion relation to see if kinetic collisions or magnetic field effects will have an influence on the coefficients or force velocity [33, 34]. Since $\omega_{Bi} << \omega_{pi}$, the effect of the magnetic field is negligible [41] and 1D wave solutions are sufficient.

Knowing that magnetic field effects are negligible, we need to assess whether ion-neutral collisions will affect soliton production. At altitudes below 400km, the neutral density exceeds the electron density [14, 42], causing ion-neutral collisions [41], so $\gamma > 0$. In general, $\gamma > 0$ in regions where the neutral density is at least three orders of magnitude greater than the electron density. At 400km, $n_n/n_e = 133$ [14], and $\gamma = 0.04$. At 200km, $n_n/n_e = 16800$ [14], and $\gamma = 4.1$. However, above 400km, n_n/n_e decreases [14], ion-neutral collisions are negligible and $\gamma = 0$. Since the dissipation coefficient $\gamma = 0$, we can assume that solitons will propagate without collisional damping in a uniform environment. In some polar regions, the plasma density is low, so the ion plasma frequency decreases and becomes comparable to the ion cyclotron frequency. In that case, the angle between the velocity and the magnetic field lines also needs to be considered. Additionally, there are some regions in low LEO where $n_i >> n_e$. In that case, $\gamma > 0$.

2.3.2 Derived Force

Orbital debris will become charged due to the electrons and ions in the plasma environment, and will create a perturbation in the electric potential and density of the surrounding plasma. We will approximate the forcing term of the fKdV equation as a function of the debris surface potential and size.

For a spherical debris object immersed in a plasma, the charge Q of the sphere is related to the capacitance C and surface potential Φ_s by:

$$Q = C\Phi_s \tag{29}$$

For a spherical particle with radius $a < \lambda_D$, the capacitance is estimated in the orbit motion limited (OML) regime as [13]:

$$C = 4\pi\epsilon_o a \tag{30}$$

We refer to Bibhas [43] for a general expression of the surface potential that can be used in a thin sheath or thick sheath domain. The radius s of the plasma sheath around a sphere is defined as:

$$s = a + \lambda_D \tag{31}$$

The surface potential of the debris (Φ_s) is calculated as [43]:

$$\exp\Big[\frac{e\Phi_s}{k_B T}\Big] = \Big(\frac{m_e}{m_i}\Big)^{1/2}\Big(\frac{s}{a}\Big)^2\left[1 - \frac{s^2 - a^2}{s^2}\exp\Big[\frac{a^2}{s^2 - a^2}\frac{e\Phi_s}{k_B T}\Big]\right] \tag{32}$$

In the thin sheath domain ($a > \lambda_D$), for a negative Φ_s, Eqn 32 simplifies to:

$$\exp\Big[\frac{e\Phi_s}{k_B T}\Big] = \Big(\frac{m_e}{m_i}\Big)^{1/2} \tag{33}$$

In the thick sheath domain ($a < \lambda_D$), Eqn 32 simplifies to:

$$\exp\Big[\frac{e\Phi_s}{k_B T}\Big] = \Big(\frac{m_e}{m_i}\Big)^{1/2}\left[1 - \frac{e\Phi_s}{k_B T}\right] \tag{34}$$

Next, we calculate the plasma potential Φ_p due to the surface potential of the debris (Φ_s) using Eqn 35, at one Debye length away from the surface of the spherical debris [44], $r = \lambda_D$. In our normalized coordinate system, plasma potential is divided by the electron temperature, as shown in Eqn 36:

$$\Phi_p = \Phi_s \exp\left[\frac{-r}{\lambda_D}\right] \tag{35}$$

$$\Phi_{p,n} = \Phi_s \exp\left[\frac{-r}{\lambda_D}\right]\left(\frac{e}{k_B T_e}\right) \tag{36}$$

Figure 1 shows the resulting calculations of the normalized plasma potential, $\Phi_{p,n}$, using Eqn 32 and Eqn 36.

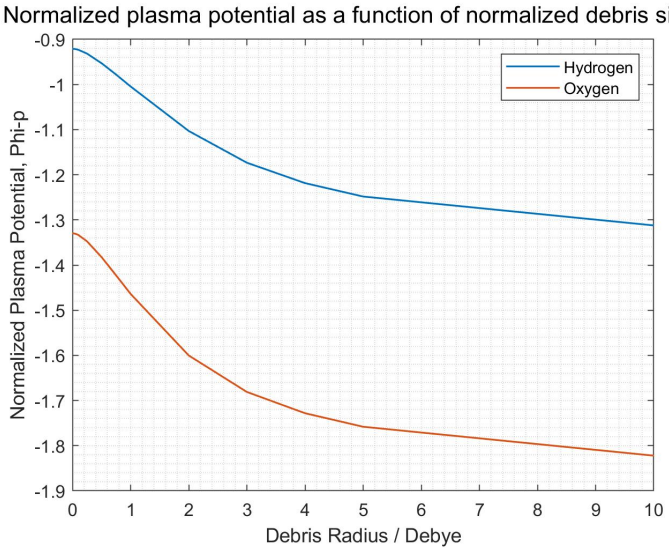

Figure 1: Normalized plasma potential, $\Phi_{p,n}$, calculated from Eqn 32, for two different dominant plasma species (oxygen and hydrogen ions).

Finally, the forcing term is estimated as a Gaussian shape with $\Phi_{p,n}$, the amplitude, and G, the full width at half maximum [45]:

$$f(\xi, \tau) = \Phi_{p,n} \exp\left[-\left(\frac{\xi - V_d \tau}{G}\right)^2\right] \tag{37}$$

where the radius of the orbital debris is normalized by λ_D:

$$G = \frac{a}{\lambda_D} \tag{38}$$

2.3.3 Numerical Methods

Two independent pseudospectral schemes were used to simulate the solitons. These two methods, developed by Fornberg & Whitham (FW) [46] and Chan & Kerkhoven (CK) [47], use Fourier transforms of the fKdV terms. While there are many examples of these methods with the unforced KdV equation, there are few that describe their application to the forced KdV equation. We apply the Fourier transform to the forcing function as prescribed by Shen [31]. The two schemes were written in Matlab and applied to known analytic solutions to the fKdV [32, 48, 45], and the results are provided in Section 2.4. Note that while Shen [31] includes a $\sqrt{N}$ factor to visualize a Dirac forcing term, the $\sqrt{N}$ factor is specific to the Shen example and should not be used in the approximation of the analytic solutions in Section 2.4, or the orbital debris simulations.

For both FW and CK schemes, the spatial domain $[-L, L]$ is discretized into N equidistant points and is normalized to $[0, 2\pi]$. Now, $\Delta\xi = \frac{2\pi}{N}$ and $\xi = s(x + L)$, where $s = \frac{\pi}{L}$ so that the solution is periodic from 0-2π. The resulting normalized fKdV equation is:

$$\frac{\partial U}{\partial \tau} + \alpha s U \frac{\partial U}{\partial \xi} + \beta s^3 \frac{\partial^3 U}{\partial \xi^3} = \frac{1}{2} s \frac{\partial f}{\partial \xi} \tag{39}$$

The time derivative in both FW and CK schemes is expressed as a finite difference approximation:

$$\frac{\partial U_j}{\partial \tau} \approx \frac{1}{2\Delta\tau}(U_j^{n+1} - U_j^{n-1}) \tag{40}$$

where the subscripts are the spatial domain and the superscripts are in the temporal domain. Thus, $j = \Delta\xi$, $n+1 = \tau + \Delta\tau$, and $n-1 = \tau - \Delta\tau$.

The discrete Fourier transform is:

$$\hat{U} = \mathscr{F}(U) = \frac{1}{\sqrt{N}} \sum_{j=0}^{N-1} U_j e^{(-2\pi jk/N)i} \qquad k = -\frac{N}{2}, -\frac{N}{2}+1, ..., \frac{N}{2}-1 \tag{41}$$

where $\mathscr{F}$ is the Fourier transform, and $\mathscr{F}^{-1}$ is the inverse Fourier transform.

An important property of the Fourier transform is that it represents differentiation as multiplication by ik, since the partial derivative commutes.

$$\mathscr{F}\Big(\frac{\partial U}{\partial \xi}\Big) = \int_{-\infty}^{\infty} \Big(\frac{\partial U}{\partial \xi}\Big) e^{-ik\xi}\, \mathrm{d}\xi = -\int_{-\infty}^{\infty} U\Big(\frac{\partial e^{-ik\xi}}{\partial \xi}\Big)\, \mathrm{d}\xi = ik\int_{-\infty}^{\infty} U e^{-ik\xi}\, \mathrm{d}\xi \tag{42}$$

In the FW scheme, the Fourier transforms are applied to the spatial derivatives:

$$U\mathscr{F}^{-1}(\mathscr{F}\frac{\partial U}{\partial \xi}) = U\mathscr{F}^{-1}(ik\mathscr{F}(U)) \tag{43}$$

$$\mathscr{F}^{-1}(\mathscr{F}\frac{\partial^3 U}{\partial \xi^3}) = \mathscr{F}^{-1}((ik)^3\mathscr{F}(U)) \tag{44}$$

Applying Eqn 40 and Eqn 43-Eqn 44 to Eqn 39 results in the following for the FW scheme:

$$\frac{1}{2\Delta t}(U^{n+1} - U^{n-1}) + \alpha U s\mathscr{F}^{-1}(ik\mathscr{F}(U)) + \beta s^3\mathscr{F}^{-1}((ik)^3\mathscr{F}(U)) = \frac{1}{2}s\mathscr{F}^{-1}(ik\mathscr{F}(f)) \tag{45}$$

After rearranging terms, the solution for U using the FW scheme is:

$$U^{n+1} = U^{n-1} - 2\Delta t\alpha U s\mathscr{F}^{-1}(ik\mathscr{F}(U)) - 2\Delta t\beta s^3\mathscr{F}^{-1}(i^3k^3\mathscr{F}(U)) + \Delta t s\mathscr{F}^{-1}(ik\mathscr{F}(f)) \tag{46}$$

The Chan-Kerkhoven scheme uses a leapfrog finite difference method in the spectral space, thereby reducing the number of Fourier transforms required for each time step. Thus, Chan-Kerkhoven is recognized as the fastest method to date for solving the KdV equations [49]. The approximations for the dispersion term is:

$$\frac{\partial^3 U}{\partial \xi^3} \approx \frac{1}{2}\frac{\partial^3 (U_j^{n+1} + U_j^{n-1})}{\partial \xi^3} \tag{47}$$

$$\mathscr{F}^{-1}(\mathscr{F}\frac{\partial^3 U}{\partial \xi^3}) \approx \mathscr{F}^{-1}((ik)^3\frac{1}{2}\mathscr{F}(U_j^{n+1} + U_j^{n-1})) \tag{48}$$

The nonlinear term becomes:

$$\mathscr{F}^{-1}(\mathscr{F}\frac{\partial U^2}{\partial \xi}) \approx \mathscr{F}^{-1}(iks\mathscr{F}(U_j^n)^2) \tag{49}$$

Applying Eqn 48 and Eqn 49 to Eqn 39 results in the following for the CK scheme:

$$\frac{1}{2\Delta t}(U^{n+1} - U^{n-1}) + \alpha\mathscr{F}^{-1}(iks\mathscr{F}(U^n)^2) + \beta s^3\mathscr{F}^{-1}(i^3k^3\frac{1}{2}\mathscr{F}(U^{n+1} + U^{n-1})) = \frac{1}{2}s\mathscr{F}^{-1}(ik\mathscr{F}(f)) \tag{50}$$

After rearranging terms, the solution for U using the CK scheme is:

$$U^{n+1} = \mathscr{F}^{-1}\Big[\frac{1}{1 - \Delta t\beta i s^3k^3}((1 + \Delta t\beta i s^3k^3)\mathscr{F}(U^{n-1}) - \Delta t\alpha isk\mathscr{F}(U^n)^2 + \Delta tisk\mathscr{F}(f))\Big] \tag{51}$$

For the testing of the analytic solutions provided in Section 2.4, an average 10^{-9} difference in the peak soliton heights averaging 1.5 in amplitude was found between FW and CK techniques, for a 6x10^{-8} percent difference between the two codes. Since CK is computationally faster than FW, the orbital debris simulations provided were generated using the CK method.

To implement the code, we first define the input parameters α, β, N, L, V_d, $\Phi_{p,n}$, G, $\Delta\tau$, τ_0, and τ_{final}. Next, we define the mesh space, ξ, and the wave numbers, k. For narrow forcing functions, it is important that the shape of the Gaussian is well defined with the given mesh size so that the force will propagate appropriately as it translates in space. Increasing N to accommodate a narrow forcing function and large τ_{final} may result in exponentially larger computation times. One may consider defining a smaller L and non-periodic boundary so that the wave solution does not wrap from the right to left spatial boundaries. It has been theorized that the precursor solitons comes solely from the depression zone between the upstream and downstream regions [32]. Thus, when simulating precursor solitons and defining non-periodic boundaries, it is important to ensure that L is sufficient so that the depression zone between the upstream and downstream regions, as well as the upstream of the solitons, are well defined, as illustrated in Figure 2.

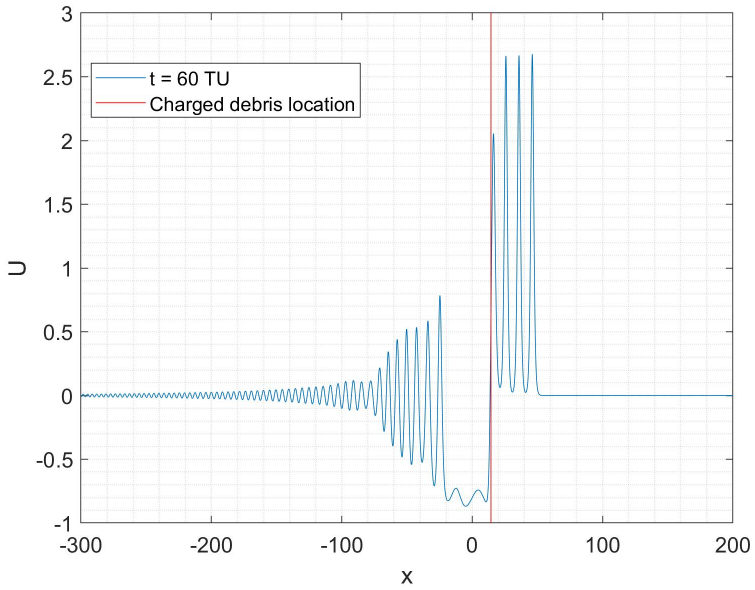

Figure 2: Example of depression zone ($-20 < x < 10$) between downstream wake ($x < -20$) and upstream precursor solitons ($x > 10$).

The solution for U is then marched forward in time using Eqn 51. For large propagation times, it is recommended to store every 100th or 1000th solution for U and the time vector into a matrix. Since the CK pseudospectral method requires information from the previous time step, we are required to define the initial wave, U_0 at τ_0. To simulate from a rest state, initialize $U = 0$ and then march forward in time with Eqn 51, using a small time step $\Delta\tau/10$ to grow the wave for ten steps to remove any numerical instabilities for the initial approximation of U_0 [31]. The total time at this point is now $\Delta\tau$. Once U_0 is obtained, the code marches forward in time using Eqn 51 and $\Delta\tau$ to τ_{final}. To simulate analytically derived pinned solitons, it is important to initialize U with the soliton solution at $t = 0$ and $t = -\Delta\tau$. As shown in Figure 8-Figure 9 in Section 2.4, a pinned soliton will not propagate in the numerical simulation unless its analytic solution is defined at U_0.

2.4 Code Validation

This section describes the validation of the numerical simulation described in Section 2.3.3. Several analytical solutions for the forced and unforced KdV equations were chosen with a variety of input parameters.

Differences between the numerical and analytical solutions were calculated in order to assess accuracy of the code.

The code was first tested on an unforced analytic solution from [22], with the input parameters in Table 3 and initial condition $U_0 = 12\text{sech}^2(x)$. This solution falls within the family of exact N-soliton solutions of the form in Eqn 52 [50], with $N = 3$. The 3-soliton solution was produced as expected, and shown in Figure 3.

$$U(x,0) = N(N+1)\text{sech}^2(x) \tag{52}$$

Table 3: Input parameters for 3-soliton analytic solution from [22].

α	β	N	L	dt
6	1	1024	50	0.001

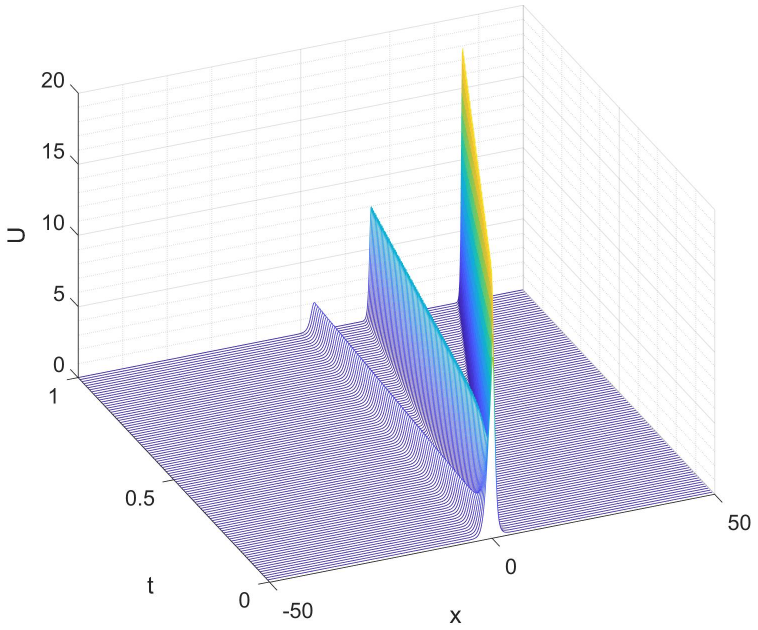

Figure 3: Reproduction of unforced 3-soliton solution from [22]. The initial condition is $12\text{sech}^2(x)$, with $\alpha = 6$ and $\beta = 1$.

Once the code was validated against an unforced KdV analytic solution, we proceeded with several forced KdV analytic solutions of various coefficients, propagation times, and forcing terms that are either static or change with space and time.

Two analytic forced KdV solutions were tested from [48]. The forcing term for both examples is given as Eqn 53, and the solution is given as Eqn 54.

$$f(x,t) = \frac{12k\beta}{\alpha}\big(k^3(4\beta - \delta) - \frac{\partial a(t)}{\partial t}\big) \tag{53}$$

$$U(x,t) = 12\beta k^2\text{sech}^2\big(k(x - \delta k^2 t) - a(t)\big) \tag{54}$$

For the example in Figure 4, $a(t)$ is defined as $a(t) = \exp\big(b_2 t^2 + b_1 t + b_0\big)$, where b_2, b_1, and b_0 are constants. This results in the traveling-wave forcing term in Eqn 55, with the resulting wave solution in Eqn 56. It is important to initialize the numerical simulation with the analytical solution of the wave in Eqn 56 at $t = 0$. The input parameters for Figure 4 are provided in Table 4. As expected, difference between the numerical and analytic solution is on the order of $\Delta t = 10^{-4}$s due to the discretized addition of the forcing function at each time step.

$$f(x,t) = \frac{12k\beta}{\alpha}\Big(k^3(4\beta-\delta) - (2b_2t+b_1)\exp(b_2t^2+b_1t+b_0)\Big)\mathrm{sech}^2(k(x-\delta k^2t) - \exp(b_2t^2+b_1t+b_0)) \quad (55)$$

$$U(x,t) = 12\beta k^2\mathrm{sech}^2\big(k(x-\delta k^2t) - \exp\big(b_2t^2+b_1t+b_0\big)\big) \quad (56)$$

Table 4: Input parameters for the analytic solution described Eqn 55 and Eqn 56 plotted in Figure 4.

k	δ	α	β	b_1	b_0	b_2
1	4	-2	1/6	2	-1	-1

For the example in Figure 5, $a(t)$ is defined as $a(t) = b_2\arctan(At) + b_1t + b_0$, where b_2,b_1,b_0, and A are constants. This results in the dromion forcing term in Eqn 57, with the resulting wave solution in Eqn 58. It is important to initialize the numerical simulation with the analytical solution of the wave in Eqn 58 at $t = 0$. The input parameters for Figure 5 are provided in Table 5. As expected, difference between the numerical and analytic solution is on the order of $\Delta t = 10^{-4}$s due to the discretized addition of the forcing function at each time step.

$$f(x,t) = \frac{12k\beta}{\alpha}\Big(k^3(4\beta-\delta) - \frac{bA}{1+A^2t^2} - b_1\Big)\mathrm{sech}^2(k(x-\delta k^2t) - (b\arctan(At) + b_1t + b_0)) \quad (57)$$

$$U(x,t) = 12\beta k^2\mathrm{sech}^2\big(k(x-4k^2t) - (b\arctan(At) + b_1t + b_0)\big) \quad (58)$$

Table 5: Input parameters for the analytic solution described Eqn 57 and Eqn 58 plotted in Figure 5.

k	A	δ	α	β	b_1	b_0	b
1	3	4	2	1/4	-3	0	-1

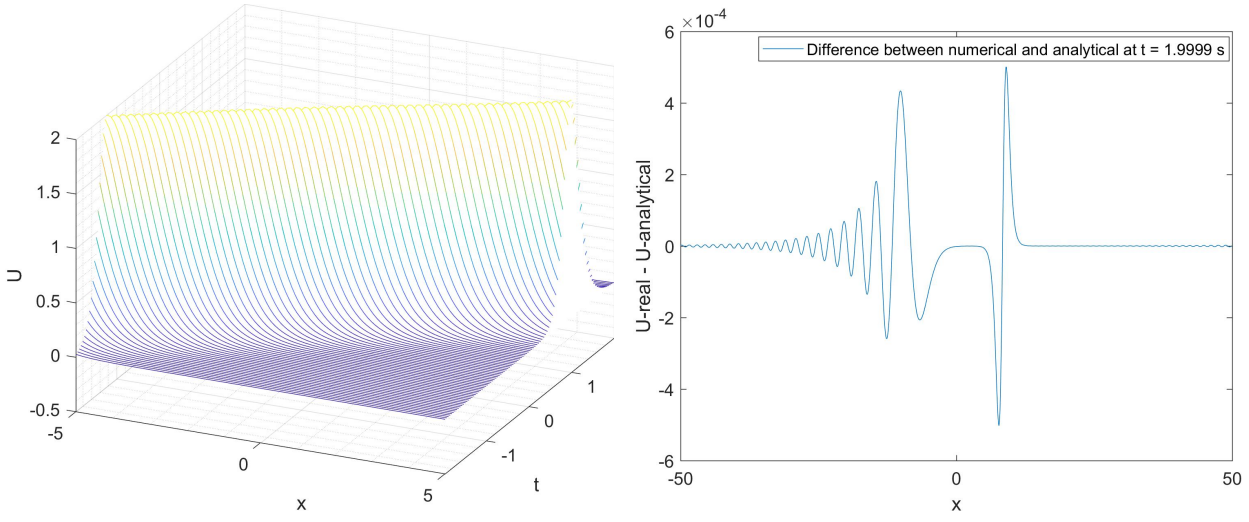

Figure 4: Reproduction of an analytic solution from Xiao et al., from a moving hyperbolic secant force defined as Eqn 55 and solution defined as Eqn 56 [48]. On the right, the accuracy of the numerical solution is limited by the discretized addition of the forcing function at each time step, so the difference between the numerical and analytic solution is on the order of $\Delta t = 10^{-4}$s.

For the next test, we reproduced the wave solution generated by a static Dirac forcing term from Shen [31]. The forcing term is a Dirac function with an amplitude = 1 and velocity = 0. The steepening, dissipation,

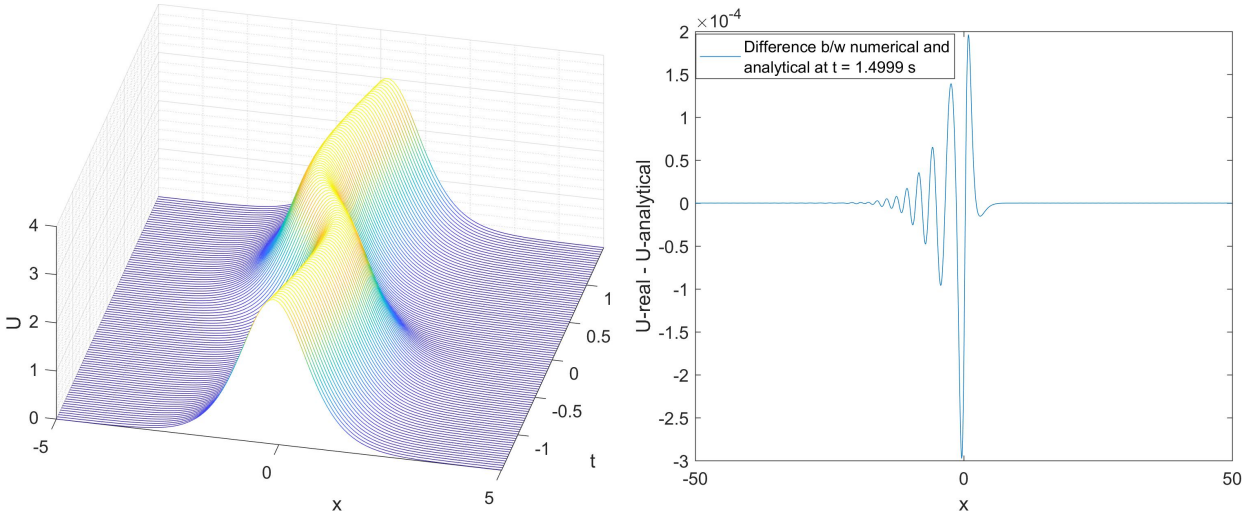

Figure 5: Reproduction of an analytic solution from Xiao et al., from a moving hyperbolic secant force defined as Eqn 57 and solution defined as Eqn 58 [48]. On the right, the accuracy of the numerical solution is limited by the discretized addition of the forcing function at each time step. The difference between the numerical and analytic solution is on the order of $\Delta t = 10^{-4}$s.

and dispersion coefficients are $\alpha = -3/2$, $\gamma = 0$, and $\beta = -1/6$ respectively. The solution is initialized from rest, $U_0 = 0$, and is propagated for 15 seconds. The results are shown in Figure 6 on the left, with one minute increments overplotted with a y-axis bias to show the wave progression. Due to negative coefficients, the upstream precursors are located on the left of the depression zone, and the wake is on the right side of the depression zone. Shen [31] published the Mathematica code for the Dirac force example. In Figure 6, the difference between the published Shen results and our numerical solution is less than 10^{-14} for solitons with maximum amplitude of 2.

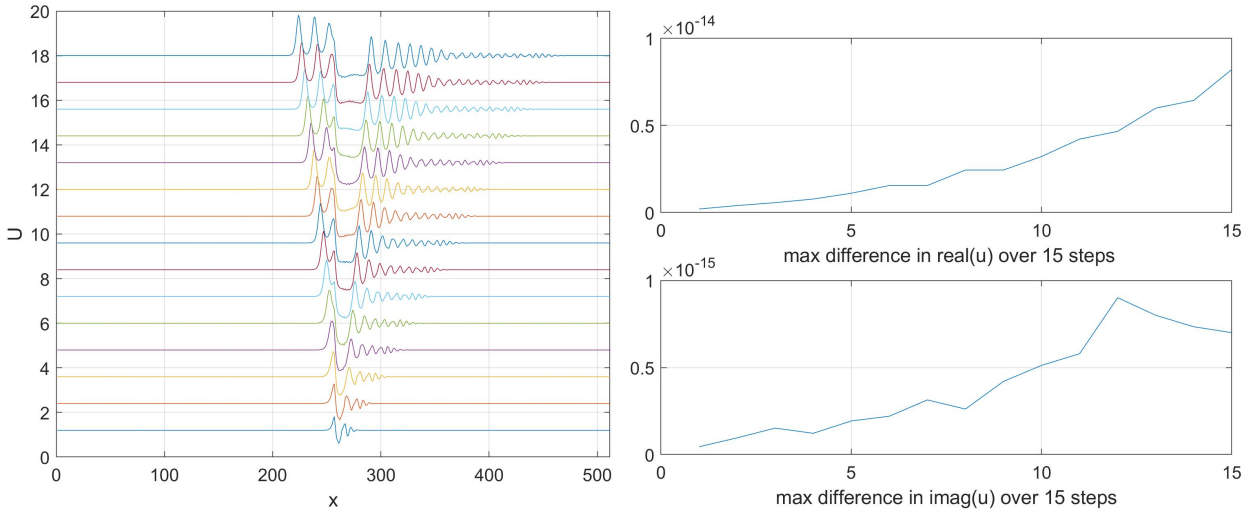

Figure 6: Left: Reproduction of forced KdV solution from Shen [31]. The force is a Dirac function with an amplitude = 1 and velocity = 0. The coefficients $\alpha = -3/2$, $\gamma = 0$ and $\beta = -1/6$. The solution is propagated for 15 seconds on the left. Due to negative coefficients, the upstream precursors are located on the left of the depression zone, and the wake is on the right side of the depression zone. Right: The difference between the published Shen results and our numerical solution is less than 10^{-14} for solitons with maximum amplitude of 2.

A pinned soliton solution was tested for the forced KdV equation [2]. Pinned solitons move at the same speed as the forcing term. The forcing term in this example is provided in Eqn 59, and the solution in Eqn 60, with $A = 20$ and $G = 1/2$. Results are shown in Figure 7. The solid blue lines, with an amplitude of 10, represent the forcing term moving to the right over time. The red lines are the soliton solution, with an amplitude of 20, moving at the same speed as the force.

$$f(x,t) = A\text{sech}^2\left[\sqrt{\frac{A}{6}}\left(x - \frac{2A - 3G}{6}t\right)\right] \tag{59}$$

$$U(x,t) = AG\text{sech}^2\left[\sqrt{\frac{A}{6}}\left(x - \frac{2A - 3G}{6}t\right)\right] \tag{60}$$

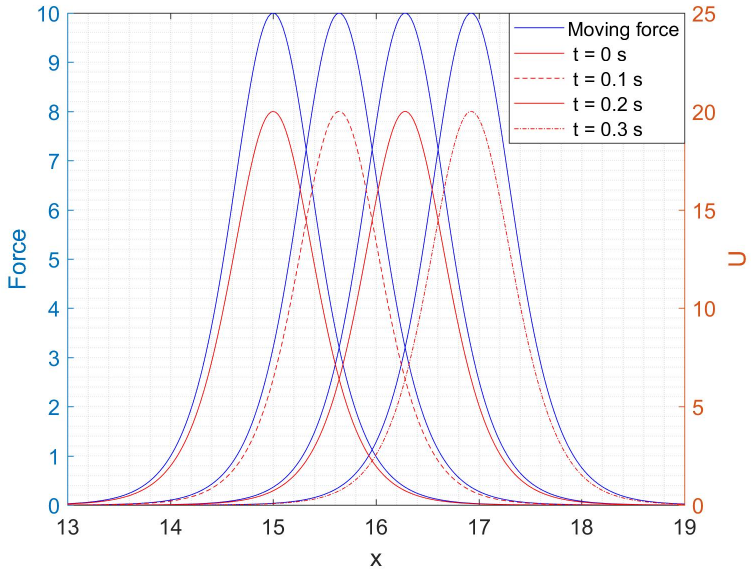

Figure 7: Reproduction of pinned soliton solution in Eqn 60 from Sen et al. [2], for a hyperbolic secant force defined in Eqn 59. The solid blue lines, with an amplitude of 10, represent the forcing term moving to the right over time. The red lines are the soliton solution, with an amplitude of 20, moving at the same speed as the force.

Another pinned soliton solution was modeled from Wu [32], and the results are shown in Figure 8. The force is $f(x) = 2b_1\text{sech}(Kx)^2$, where $b_1 = -0.1250$ and $K = 0.6124$. The pinned soliton is initialized at U_0 with its solution of $U(x) = a\text{sech}(Kx)^2$, where $a = 0.5$. The difference between the numerical and analytical solutions are shown on the right hand side of Figure 8. The solution is highly stable, with the difference between the numerical and analytical solutions on the order of 10^{-9} for a soliton with amplitude = 0.5.

The pinned soliton solution from Wu [32] shown in Figure 8 was also modeled from rest. Using the same forcing function, the difference with initializing U_0 with the analytical solution, Figure 8, or initializing from rest with $U_0 = 0$, Figure 9, was successfully reproduced.

Finally, two examples from Grimshaw [45] using a Gaussian force were successfully reproduced. The Gaussian force is of the form in Eqn 37. For both examples in Figure 10, $G = 2$ and $V_d = 0$. For the left plot, $\Phi_{p,n} = 0.01$. For the right plot, $\Phi_{p,n} = 0.1$. The agreement between the numerical and analytical results presented here demonstrate that the simulation method is working properly.

2.5 Orbital Debris Simulation Results

Having validated our simulations of the fKdV equation and the resulting soliton solutions, we now simulate solitons using ionospheric plasma and orbital debris characteristics. Using the CK method in Eqn 51 and

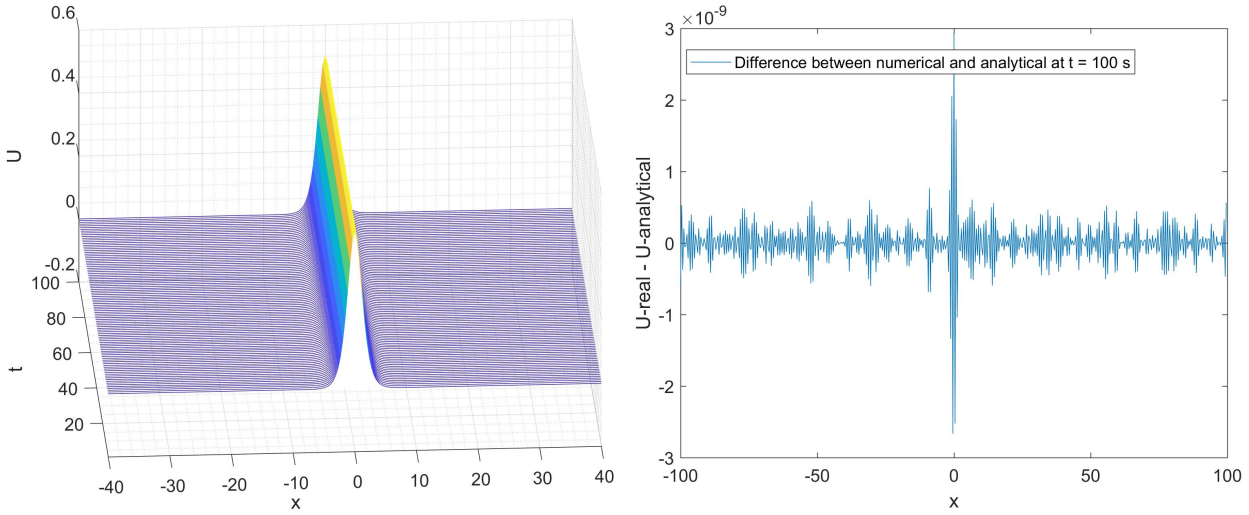

Figure 8: Reproduction of Wu [32] pinned soliton solution. The force is $f(x) = 2b_1\text{sech}(Kx)^2$, where $b_1 = -0.1250$ and $K = 0.6124$. The pinned soliton is initialized with its solution of $U(x) = a\text{sech}(Kx)^2$, where $a = 0.5$. The solution is highly stable, with the difference between the numerical and analytical solutions on the order of 10^{-9} for a soliton with amplitude = 0.5.

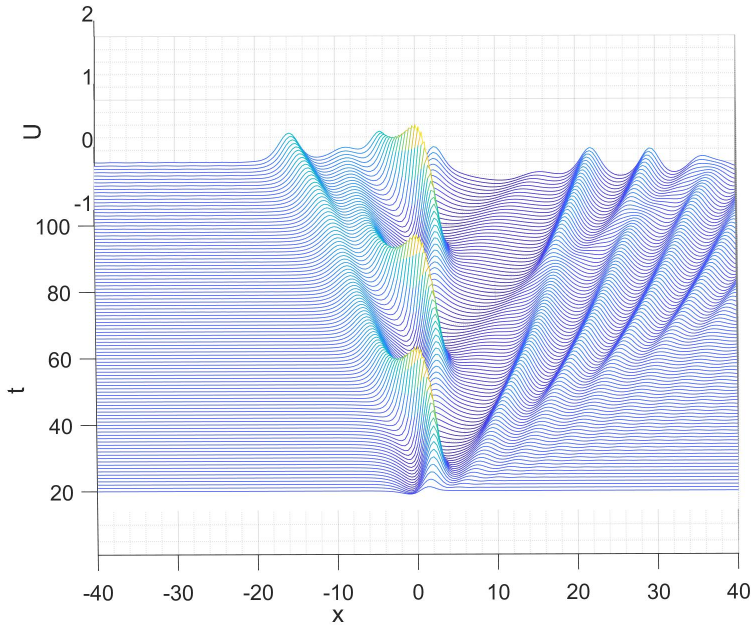

Figure 9: Reproduction of Wu [32] pinned soliton solution, similar to the previous figure. However, instead of initializing from the pinned soliton solution, the scheme is started from a rest state.

the forcing function in Eqn 37, we simulated the response of the plasma to a charged debris object for the plasma regions in Table 1 and debris radii ranging from $0.1 - 10$ cm, for a maximum propagation time of 1800 TU. The coefficients used are provided in Eqn 28. The circular orbit velocity from Table 1 was used for the debris velocity. Note that as G decreases, L and N are adjusted to ensure that the force is sufficiently resolved as it is propagated with time, and that the wave does not reflect across periodic boundaries in the pseudospectral scheme. The domain in these simulations is normalized as in Eqn 7. For all figures in this section, the x domain is in units of the Debye length, and time is units of Debye length divided by the ion acoustic velocity (one time unit (TU) is λ_D/V_{ia}).

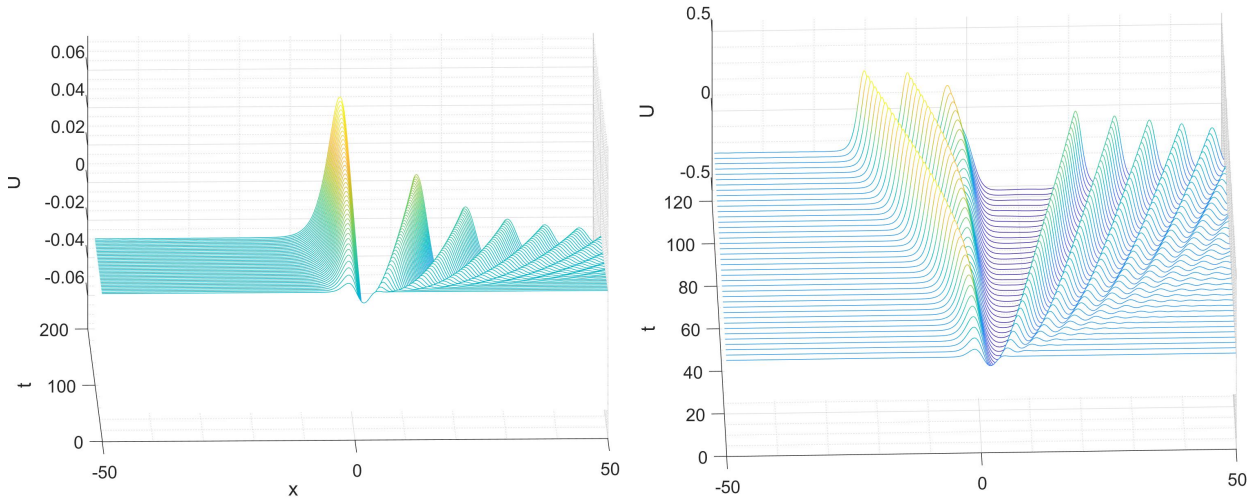

Figure 10: Reproduction of Grimshaw numerical simulation [45]. The Gaussian force is of the form in Eqn 37, with $V_d = 0$ and $G = 2$. Left: $\Phi_p = 0.01$. Right: $\Phi_p = 0.1$.

2.5.1 Low LEO

Low energy, high density plasma is found in the mid-latitude regions of LEO. The dominant ion species is O+. The debris orbital velocity is much faster than the ion acoustic velocity, and the debris size may be in either the thick sheath or thin sheath domain, depending on the plasma density. In this regime, pinned solitons were produced, traveling at the same speed as the orbital debris, as shown in Figure 11. The example shown in Figure 11 is a thin sheath (although the potential is calculated using Eqn 32), since the debris size is greater than the Debye length. Since pinned solitons travel with the debris, they are not useful for mapping efforts since they would not be sensed prior to collision. For the Low LEO region specified in Table 1 and a circular orbit velocity of 7.51 km/s, pinned solitons were observed for the full range of debris sizes (0.1 - 10cm) examined.

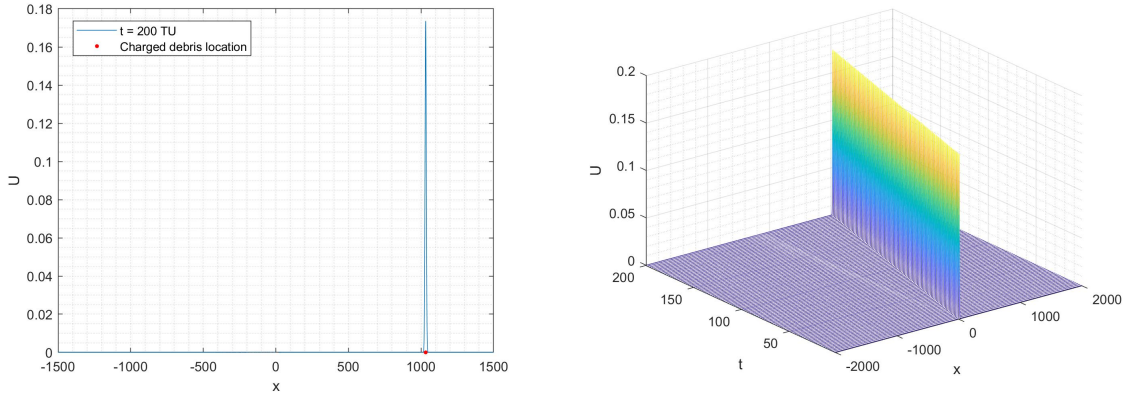

(a) Instantaneous Debris and Soliton Signature

(b) Soliton Propagation with Time

Figure 11: Pinned soliton created by 10 cm diameter charged debris in Low LEO region of Table 1, and a circular orbit velocity of 7.51 km/s, $\Phi_{p,n} = -1.77$, and coefficients $\alpha = 1.0051, \beta = 0.4925, \gamma = 0$.

2.5.2 High LEO Region 1

As the altitude increases from mid-latitude low LEO, the plasma density decreases. In this topside ionosphere environment, the dominant ion species is H+, which is much lighter than O+. The ion acoustic velocity is comparable to the debris orbital velocity, and the Debye length is comparable to the debris size. Precursor solitons are produced, advancing ahead of the debris, as shown in Figure 12 and Figure 14.

Figure 12 and Figure 14 show the solitons generated by 5mm and 1cm debris using the κ-distribution coefficients in Eqn 28, $\alpha = 1.0051$, $\beta = 0.4925$, $\gamma = 0$, while Figure 13 shows a comparison to the Maxwellian distribution coefficients, $\alpha = 1$, $\beta = 0.5$, $\gamma = 0$. Using the κ distribution results in more wave steepening and less wave dissipation, allowing for more precursor solitons to be produced in the 1400TU simulation time shown.

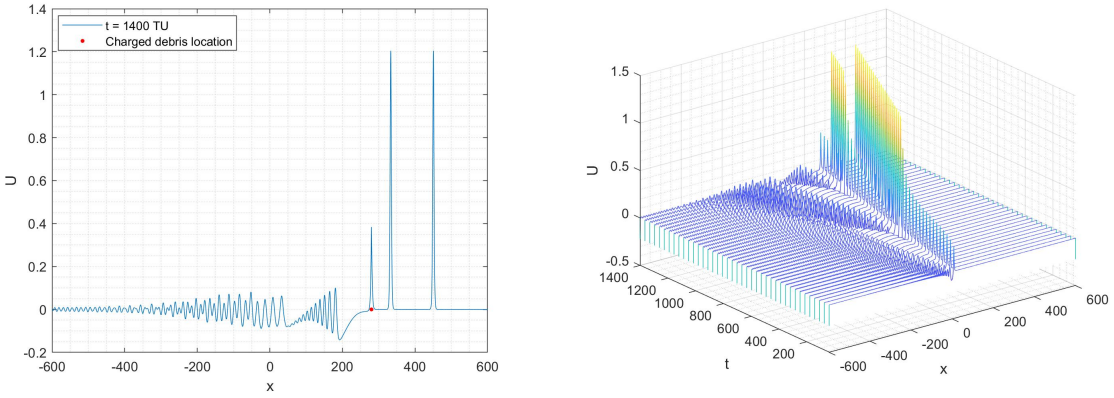

(a) Instantaneous Plasma Response

(b) Time Varying Plasma Response

Figure 12: Precursor solitons created by 5 mm diameter charged debris in High LEO Region 1 of Table 1, in an elliptical orbit with $V = 1.2V_{ia}$, $\Phi_{p,n} = -0.93$, and coefficients $\alpha = 1.0051, \beta = 0.4925, \gamma = 0$.

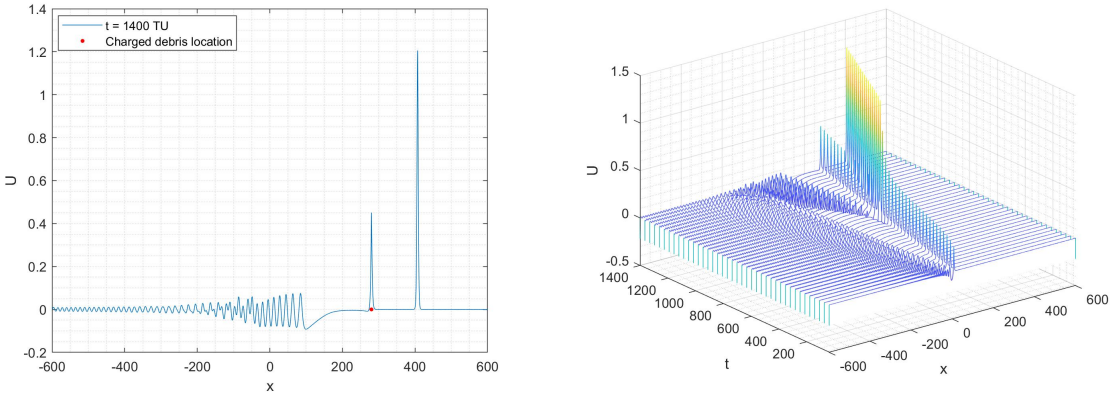

(a) Instantaneous Plasma Response

(b) Time Varying Plasma Response

Figure 13: Precursor solitons created by 5 mm diameter charged debris in High LEO Region 1 of Table 1, in an elliptical orbit with $V = 1.2V_{ia}$, $\Phi_{p,n} = -0.93$, and with Maxwellian coefficients $\alpha = 1, \beta = 0.5, \gamma = 0$.

2.5.3 High LEO Region 2

In this region, the lower limit to the topside ionosphere plasma density is used. Precursor solitons are produced, advancing ahead of the debris, as shown in Figure 15. While the ion acoustic velocity is still

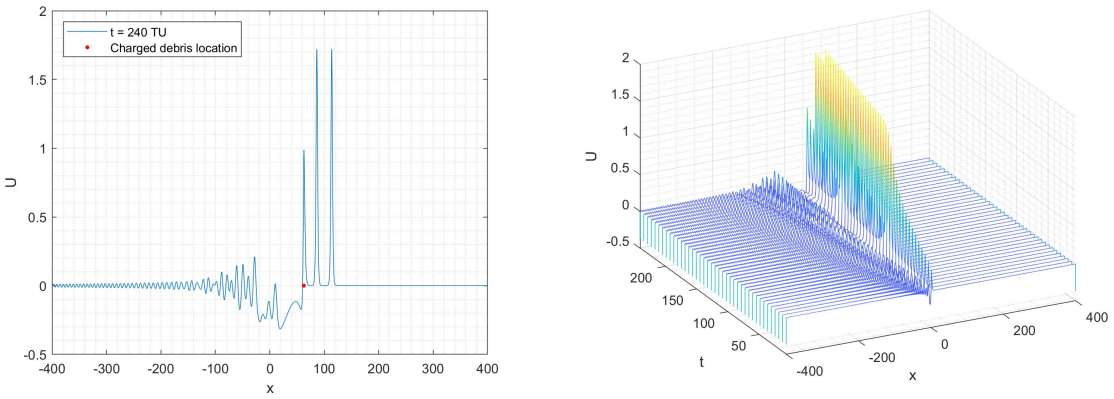

(a) Instantaneous Plasma Response (b) Time Varying Plasma Response

Figure 14: Precursor solitons created by 1 cm diameter charged debris in High LEO Region 1 of Table 1. The debris has a circular orbit velocity of 7.26 km/s, with $\Phi_{p,n} = -0.94$, and with coefficients $\alpha = 1.0051, \beta = 0.4925, \gamma = 0$.

comparable to the debris orbital velocity, the Debye length is increasingly larger than the debris size.

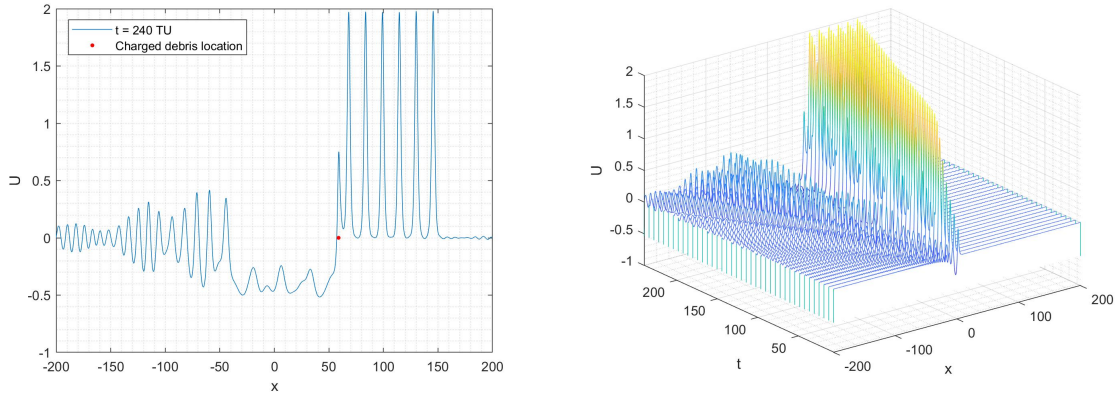

(a) Instantaneous Plasma Response (b) Time Varying Plasma Response

Figure 15: Precursor solitons created by 5 cm diameter charged debris in High LEO Region 2 of Table 1. The debris has a circular orbit velocity of 7.16 km/s, $\Phi_{p,n} = -0.96$, and coefficients $\alpha = 1.0051, \beta = 0.4925, \gamma = 0$.

2.5.4 Polar LEO

For Polar LEO 1, the plasma in this region is high energy and low density. As a result, the ion acoustic velocity exceeds the debris orbital velocity, and the Debye length is much larger than the debris size. The forcing function in Eqn 37 approaches a Dirac function moving downstream with respect to the plasma. It is possible to generate ion acoustic waves with a Dirac function with a speed comparable to the plasma speed. However, the debris speed in this case is much slower than the plasma speed. Over the full range of sizes considered and the circular orbit velocity of 7.56 km/s for Polar LEO 1 in Table 2, low amplitude perturbations are present, but no coherent waves were produced, as shown in Figure 16. Similar to Low LEO, pinned solitons are produced in Polar LEO 2, since the orbital debris velocity is much greater than the ion acoustic velocity. Precursor solitons are generated in Polar LEO 3, since the orbital debris velocity is comparable to the ion acoustic velocity. However, the range of velocities that can produce precursor solitons

is reduced since the Debye length is greater in Polar LEO 3 when compared to High LEO 1 and High LEO 2. These limits are further discussed in Section 2.6.

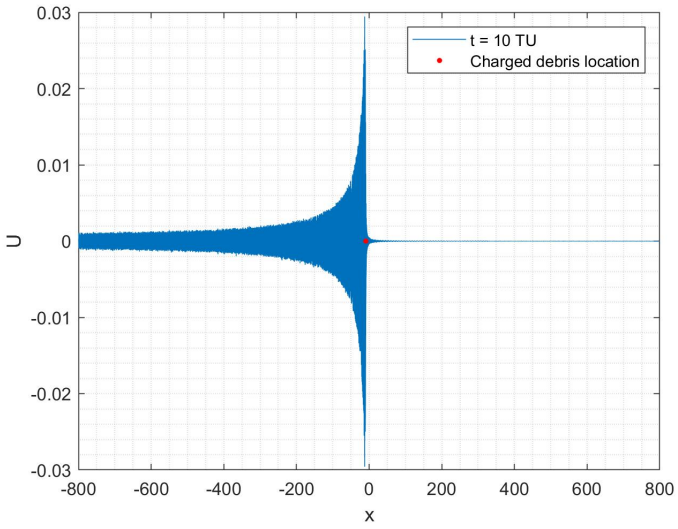

Figure 16: Dirac disturbance approximating a 1 cm diameter debris object moving slower than plasma medium, at a circular orbit velocity of 7.56 km/s, $\Phi_{p,n} = -0.92$, in Polar LEO 1. No solitons are produced.

2.5.5 GEO

Like the Polar LEO 1, the plasma environment at GEO consists of high energy, low density electrons. The ion acoustic velocity is much larger than the debris orbital velocity, and the Debye length is much larger than the debris size. Similar to results in the Polar LEO 1, no waves were produced, as shown in Figure 17.

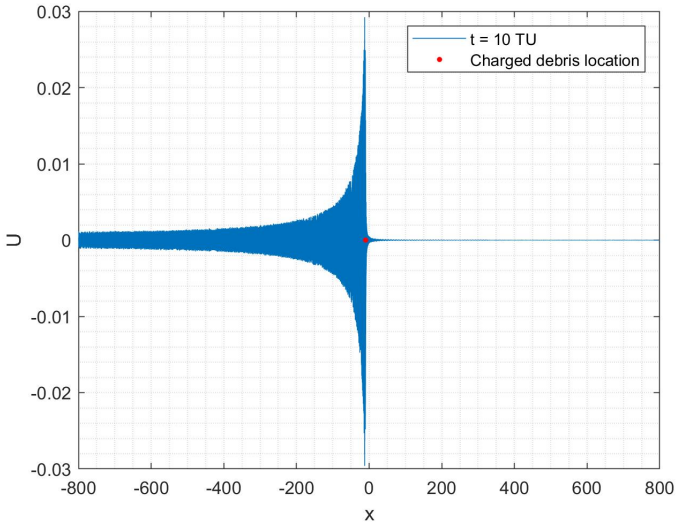

Figure 17: Dirac disturbance approximating a 1 cm diameter debris object moving slower than plasma medium, at a circular orbit velocity of 3.08 km/s, $\Phi_{p,n} = -0.92$,in GEO. No solitons are produced.

2.6 Discussion

The ability for orbital debris to produce pinned or precursor solitons depends on the relative velocity between the debris and the plasma medium. The velocity thresholds required for soliton production can be derived from Eqn 20, and solving for μ, the velocity of the plasma medium moving over a static disturbance. The derivation also applies to a static plasma medium and a moving disturbance, or in general, the relative velocity between the plasma and the disturbance [31]. In order to produce pinned solitons, the debris velocity must be supercritical, and $U(0) = U(\infty)$. No solitons are produced at subcritical velocities where $U(0) = U(\infty) = 0$. The transcritical regime, where precursor solitons are produced, resides between the subcritical and supercritical velocity limits.

In the transcritical regime, the velocity of the debris that can produce precursor solitions is usually referenced in literature as $1 - 1.5$x the velocity of the medium [2, 45]. This estimation can further be refined by deriving the velocity limits at the subcritical and supercritical boundaries. Assuming that $U(0) = U(\infty)$, Eqn 20 leads to a relationship between the area of the forcing disturbance, steepening coefficient, and dissipation coefficient [31, 51]:

$$V_{sup} = 1 + \left(\frac{3(\alpha/2)^2 A^2}{16\beta} \right)^{1/3} \tag{61}$$

Where the area of the Gaussian forcing disturbance is:

$$A = |\Phi_{p,n}| G \sqrt{\pi} \tag{62}$$

Recall that the spatial domain, x, and the debris width, G, are normalized by the Debye length according to Eqn 7 and Eqn 38. The normalized plasma potential,$\Phi_{p,n}$, is nondimensionalized by the electron temperature, according to Eqn 36.

Thus, for a 1 cm diameter debris in High LEO Region 1 and Debye length of 1.38 cm, the supercritical velocity limit is $V_{sup} = 1.33 V_{ia}$ [31]. For 1 cm diameter debris in High LEO Region 1, the subcritical velocity limit is calculated using Eqn 63 and $V_{sub} = 0.48 V_{ia}$. Note that the velocity threshold is proportional to the area of the forcing function. Smaller debris will have a smaller transcritical velocity range, and larger debris will have a larger transcritical velocity range. For debris with 1/2 cm diameter in High LEO Region 1, $V_{sup} = 1.20 V_{ia}$ and $V_{sub} = 0.68 V_{ia}$. The supercritical and subcritical velocities for the regions in Table 1 and Table 2 are listed in Table 6 and Table 7.

$$V_{sub} = 1 - \left(\frac{3(\alpha/2)^2 A^2}{4\beta} \right)^{1/3} \tag{63}$$

In Table 6 and Table 7, the transcritical velocity limits are listed in units of the ion acoustic velocity. For $V > V_{ia}$, the debris is traveling faster than the ion acoustic velocity, along the same direction. For $0 < V < V_{ia}$, the debris is traveling slower than the ion acoustic velocity, along the same direction. For $V = V_{ia}$, the debris is static with respect to the ion acoustic velocity. For $V < 0$, the debris is traveling in the opposite direction as the ion acoustic velocity. Examples of soliton generation with $V < 0$ are provided in Figure 18.

Orbital debris in High LEO with circular and elliptical orbits will fall within the transcritical velocity threshold for a range of sub-centimeter debris sizes. For example, the velocity of debris in circular orbit at 1,200 km altitude, $V_d = 1.26 V_{ia}$. For debris in an elliptical orbit with 1,200 km apogee and 200 km perigee, $V_d = 1.22 V_{ia}$ at 1,200 km. Precursor solitons are expected for the subset of elliptical orbits that fall within the supercritical and subcritical velocity limits in Table 6, with a wider range of orbits falling within the High LEO 1 region for mm-cm size debris. The soliton generation will be limited by the amount of time the debris spends in the H+ dominated plasma.

Numerical simulations show that sub-centimeter orbital debris produces pinned solitons in mid-latitude Low LEO regions. For circular orbits, the debris velocity is much larger than the ion acoustic velocity in Low LEO. The debris velocity is comparable to the ion acoustic velocity for circular orbits in the High LEO region, thus the creation of precursor solitons is possible in High LEO.

Table 6: Normalized plasma potential, $\Phi_{p,n}$, and orbital velocity range for 10 cm, 5 cm, 1 cm, 5 mm, and 1 mm diameter debris to produce precursor solitons in the mid-latitude ionosphere. λ_D is the plasma Debye length, V_d is the velocity of debris in a circular orbit, V_{sup} is the supercritical velocity limit, V_{sub} is the subcritical velocity limit, and V_{ia} is the ion acoustic velocity. For GEO, the dominant ion could be oxygen or hydrogen depending on solar activity, so V_{ia} is included for both species. The table has four columns (ionosphere regions). The first four rows describe the characteristics of those regions. After that, there are five groups of rows that present the debris potential and velocity limits for five different debris sizes.

	Low LEO	High LEO 1	High LEO 2	GEO
Altitude (km)	700	1200	1400	35,786
Latitude (deg)	0-55	0-55	0-55	0-90
λ_D (cm)	0.83	1.38	4.36	23,504.00
V_d (V_{ia})	6.16	1.26	1.24	0.04 / 0.01
10 cm diameter debris				
$\Phi_{p,n}$	-1.77	-1.20	-1.02	-0.92
V_{sup} (V_{ia})	4.25	2.79	1.74	1.00
V_{sub} (V_{ia})	-4.16	-1.84	-0.18	1.00
5 cm diameter debris				
$\Phi_{p,n}$	-1.68	-1.08	-0.96	-0.92
V_{sup} (V_{ia})	2.98	2.05	1.45	1.00
V_{sub} (V_{ia})	-2.14	-0.67	0.28	1.00
1 cm diameter debris				
$\Phi_{p,n}$	-1.40	-0.94	-0.92	-0.92
V_{sup} (V_{ia})	1.60	1.33	1.15	1.00
V_{sub} (V_{ia})	0.05	0.48	0.76	1.00
5 mm diameter debris				
$\Phi_{p,n}$	-1.35	-0.93	-0.92	-0.92
V_{sup} (V_{ia})	1.37	1.20	1.09	1.00
V_{sub} (V_{ia})	0.41	0.68	0.85	1.00
1 mm diameter debris				
$\Phi_{p,n}$	-1.33	-0.92	-0.92	-0.92
V_{sup} (V_{ia})	1.12	1.07	1.03	1.00
V_{sub} (V_{ia})	0.80	0.89	0.95	1.00

In our normalized system, the soliton amplitude displayed in Figure 11 - Figure 15 is the perturbed ion density normalized by the unperturbed ion density, $U = (n - n_0)/n_0$. For example, Figure 15 has a soliton amplitude of 2, corresponding to 3x the unperturbed ion density in High LEO 2. In High LEO 2, the unperturbed ion density is 10^4 cm^{-3}, so the perturbed ion density will be 3x10^4 cm^{-3}.

In this investigation, we have considered the propagation of plasma solitons in a uniform, constant plasma environment. However, the plasma environment changes with time of day and location. Future work will investigate the dissipation of solitons produced by orbital debris as those solitons encounter varying plasma environments. Solitons will propagate without collisional damping until they reach an area of turbulence or a higher energy kappa distribution, which could have a different α or β, and $\gamma > 0$. Additionally, the forcing function will change in width due to the changing Debye length at varying altitudes. Future work will investigate the propagation of solitons in regions where $\gamma = 0$ to $\gamma > 0$.

Typically, the Boussinesq equations [31] are used to describe full water wave theory, which allow for wave propagating in multiple directions, and wave influence in the transverse direction as well. However, the KdV approximation is a simplification of the Boussinesq equations and only admits waves traveling in one direction [31, 45, 32]. From the dispersion relation, it is shown that the wave is dispersive and propagates in only one direction, since there is only one sign for a given wavenumber. Using the KdV approximation, it is expected that solitons generated from orbital debris will propagate unidirectionally from the debris location [31]. Our current results model the solitons generated at the peak height of the Gaussian forcing term, but it is possible that solitons will also be generated along the width of the Gaussian as the height decreases, similar to the

Table 7: Normalized plasma potential, $\Phi_{p,n}$, and orbital velocity range for 10 cm, 5 cm, 1 cm, 5 mm, and 1 mm diameter debris to produce precursor solitons in the high-latitude ionosphere. λ_D is the plasma Debye length, V_d is the velocity of debris in a circular orbit, V_{sup} is the supercritical velocity limit, V_{sub} is the subcritical velocity limit, and V_{ia} is the ion acoustic velocity. For Polar LEO 1, the dominant ion could be oxygen or hydrogen depending on solar activity, so V_{ia} is included for both species. The table has three columns (ionosphere regions). The first four rows describe the characteristics of those regions. After that, there are five groups of rows that present the debris potential and velocity limits for five different debris sizes.

	Polar LEO 1	Polar LEO 2	Polar LEO 3
Altitude (km)	600	600	950
Latitude (deg)	55-90	55-90	55-90
λ_D (cm)	7,432.00	3.72	13.91
V_d (V_{ia})	0.1 / 0.02	6.20	1.28
10 cm diameter debris			
$\Phi_{p,n}$	-0.92	-1.51	-0.94
V_{sup} (V_{ia})	1.00	2.08	1.33
V_{sub} (V_{ia})	0.99	-0.71	0.48
5 cm diameter debris			
$\Phi_{p,n}$	-0.92	-1.41	-0.93
V_{sup} (V_{ia})	1.00	1.65	1.20
V_{sub} (V_{ia})	1.00	-0.03	0.68
1 cm diameter debris			
$\Phi_{p,n}$	-0.92	-1.34	-0.92
V_{sup} (V_{ia})	1.00	1.21	1.07
V_{sub} (V_{ia})	1.00	0.66	0.86
5 mm diameter debris			
$\Phi_{p,n}$	-0.92	-1.33	-0.92
V_{sup} (V_{ia})	1.00	1.13	1.04
V_{sub} (V_{ia})	1.00	0.79	0.93
1 mm diameter debris			
$\Phi_{p,n}$	-0.92	-1.33	-0.92
V_{sup} (V_{ia})	1.00	1.05	1.01
V_{sub} (V_{ia})	1.00	0.93	0.98

semicircular shape observed in [26] and recent ocean wave simulations [52]. To understand the 3D (2+1) propagation of solitons, future work will employ the forced Kadomtsev-Petviashvili (KP) equation, which extends the forced KdV equation into three dimensions [53, 54]. The KP equation has been demonstrated for the modeling of ion-acoustic waves in weakly magnetized or unmagnetized, cold, Maxwellian plasmas [55, 56, 57].

2.7 Summary

We have demonstrated that charged orbital debris can create pinned solitons in the O+ dominated regions of mid-latitude low LEO, and precursor solitons in H+ dominated high LEO. These precursor solitons will allow for mapping of sub-centimeter orbital debris between 800 km - 2,000 km altitude, providing a capability to characterize the orbital debris population with existing sensor technology, in a region where orbital debris estimations are not fully understood. Follow on studies will investigate the long-distance propagation of solitons through gradually varying plasma environments in the presence of additional damping processes, and 3D propagation.

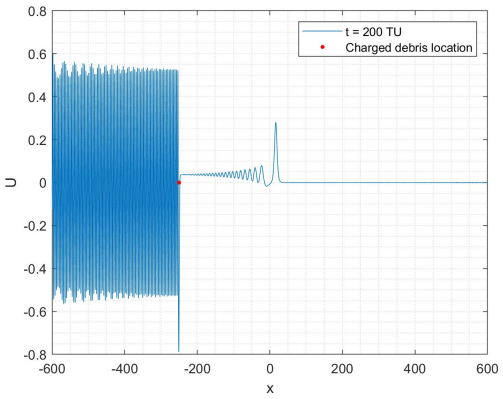

(a) Instantaneous Plasma Response

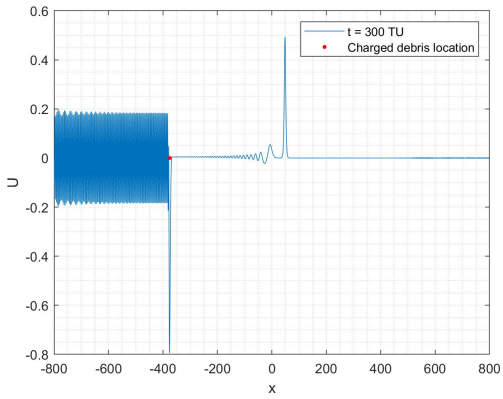

(b) Instantaneous Plasma Response

Figure 18: High LEO Region 1. (a) Solitons generated by charged debris with 5 cm diameter. The debris is traveling to the left along the x axis, $V_d = -0.25V_{ia}$ and $\Phi_{p,n} = -1.08$. (b) Solitons propagating from charged debris with 10 cm diameter. The debris is traveling to the left along the x axis, $V_d = -0.25V_{ia}$ and $\Phi_{p,n} = -1.20$.

3 CubeSat Constellation Orbit Design

In the previous section, we investigated the characteristics of solitons that are predicted to be produced by small, sub-cm orbital debris. The second, key component of assessing the feasibility of mapping orbital debris via soliton detection is to calculate the required size of the fleet of CubeSats. In order to improve upon the current witness plate method of assessing the small orbital debris environment (i.e., the Long Duration Exposure Facility that was on orbit for 5 years [58]), the fleet must be able to map the debris environment in a given small ($\approx$ 100km) altitude range in less than 1 year. However, the fleet must also not contribute to the debris problem. Thus, it is desirable that the fleet size should be as small as possible, but definitely smaller than 1000 CubeSats. As the fleet size grows larger, the time required for mapping decreases. Thus, there is a trade between fleet size and mapping frequency. It is desirable to produce debris maps quickly in order to enable assessments of the efficacy of debris remediation techniques.

As mentioned previously, a defining characteristic of plasma solitons is that they do not dissipate when propagated through a constant medium. However, the plasma environment around the Earth is time and spatially varying. Future work simulate the propagation of solitons through a spatially varying plasma medium to determine how quickly they dissipate. For the current investigation, the distance that a soliton can travel from the source debris object before becoming undetectable (henceforth, the 'detection distance') is kept as an unknown variable.

3.1 Methods

In order to calculate the time required to map the sub-cm orbital debris, we assume that the small orbital debris distribution is well approximated by the distribution of larger debris objects. The orbital elements of the currently known debris objects were downloaded from space-track.org. Rather than considering the time required to map the full debris population, we instead consider debris with ascending or descending nodes at altitudes from 400-500km (the altitude of the International Space Station), resulting in 2,311 debris objects.

We assume that the fleet of CubeSats are in equatorial orbits (inclination of 0°). Although the distance that a soliton can travel before dissipation is currently unknown, orbital mechanics tells us that all debris must be in or cross the equatorial plane. Thus, we assume that debris is detected by the fleet of CubeSats during the debris' transit across the equatorial plane. Additionally, we want to maximize the time during each CubeSat's orbit when it will be detecting debris. Thus, the CubeSat orbits were given altitudes of periapsis of 400km and altitudes of apoapsis of 500km. Lowering the altitude of periapsis or raising the altitude of apoapsis would result in a portion of the orbit where the CubeSat was outside of the region where

we are mapping debris. The longitudes of periapses for the fleet of CubeSats are equally spaced (e.g., for a fleet of five CubeSats, there would be longitudes of periapses every 72°).

The selected debris and spacecraft fleet trajectories were numerically propagated for 1 day with J2 perturbations included. J2 perturbations were included because the Earth's oblateness causes rotation of the line of apses (i.e., the perturbed orbits are not stationary, but instead rotate about the Earth, causing them to map a larger region than predicted if the orbits are assumed to be stationary). The secular J2 perturbations cause the line of nodes to regress by 7.8° per day for this orbit (note that the rate of regression will decrease with increasing semi-major axis). After propagation, the ephemerides for each piece of debris were analyzed to find equatorial plane crossings. Since the CubeSats are all on equatorial orbits, detection can only occur when the debris is at a node. After finding the first node crossing, the debris' state at the integration time step just before node crossing was used as the initial condition for Kepler's Prediction Problem (KPP). KPP takes in an initial state and predicts the location of the spacecraft at a subsequent time. KPP was used to obtain the state of the debris at small timesteps before and after the equatorial plane crossing. It is necessary to have high temporal resolution in the debris' state near the equatorial plane crossing to ensure that the 'conjunction' between the debris and a CubeSat is correctly calculated. By using KPP, we were able to generate the required high temporal resolution on the debris trajectory in the equatorial region without decreasing the timestep of the numerical integrator, which would have drastically increased the numerical integration run-time. The CubeSat population was surveyed to find all CubeSats near the debris at during the node (a.k.a. equatorial plane) crossing. KPP was the solved iteratively for the each piece of debris debris and all CubeSats within a given proximity of the debris, each time starting at the state at the integration time step just before node crossing. The timestep used in the KPP solutions was .1 seconds and allowed for precise detection within 1 km. The resulting positions of the debris and the nearby CubeSats from each KPP solution were compared to see if the debris was within the specified detection distance. This process was repeated for all node crossings for a given piece of debris. The minimum distance between the debris and the fleet over a single day was recorded. This process was completed for all 2,311 debris objects in the population. After all debris were analyzed, the final states for the CubeSats and debris populations after the 1-day propagation were used as the initial conditions for the next day of propagation. The minimum approach distance between all debris and the CubeSat population was saved for each day. Each detection of a piece of debris was categorized by its minimum approach distance (called the detection distance). Detection distances of 1 km, 1-5 km, 5-10 km, and 10-15 km were considered.

3.2 Orbit Simulation Results

We begin by calculating the number of debris objects detected considering 100 CubeSats, the largest fleet size considered acceptable for our 400-500km altitude mapping region. Figure 19 shows the percent of the debris population detected as a function of mapping duration and the detection distance. Recall that the detection distance is the distance between soliton production and its dissipation, which is currently unknown. Figure 19 shows the percent of debris that pass within some distance range of the mapping CubeSats. Thus, as the mapping duration increases, debris objects may move to lower detection distance categories. For example, a debris object that passes 12km from a CubeSat on day 7 (categorized in the 10-15km 'bin') may pass 3km from a CubeSat on day 20 (categorized in the 1-5km 'bin'). This movement of objects to lower detection distance bins is responsible for the apparent decrease in objects in the 10-15km and 5-10km bins with increasing mapping duration.

Figure 20 shows the total percent of debris objects mapped considering all detection distances less than 15km and a fleet of 100 CubeSats. Figure 20 shows that about 95% of debris can be mapped in two months, which is a vast improvement compared to the 5 year mapping duration of the LDEF [58]. Note that 90% of the debris are detected in just one month. If soliton dissipation in the varying plasma environment dictates that smaller detection distances are required, then we expect the plot the follow the same general form, but with a larger timescale.

Next we consider the effect of changing the number of CubeSats in the fleet on the time required to map the debris. Figure 21(a) shows the percent of the debris mapped in one week, assuming a 15km detection distance, for a range of fleet sizes. Figure 21(a) shows that nearly 80% of the debris from 400-500km altitude is mapped in the first week of mapping with a fleet of 100 CubeSats. Decreasing the fleet size to 50 CubeSats results in 60% of the debris mapped in the first week. Decreasing the fleet size to 10 CubeSats results in only

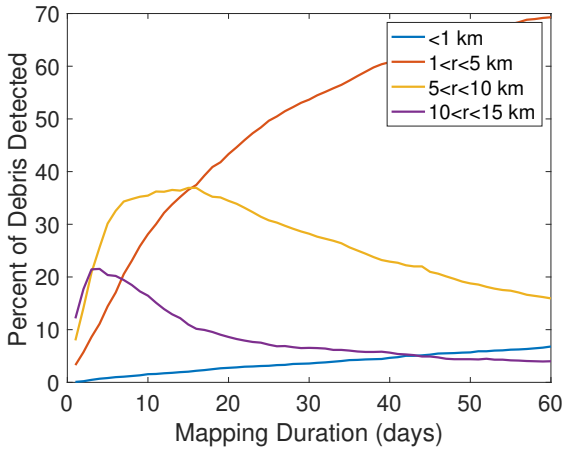

Figure 19: Percent of debris objects mapped (out of 2,311 total) from 400-500km altitude considering a fleet of 100 mapping CubeSats, as a function of mapping duration and detection distance (r). Detection distance is the maximum distance between the production of the soliton and its dissipation, which is currently unknown.

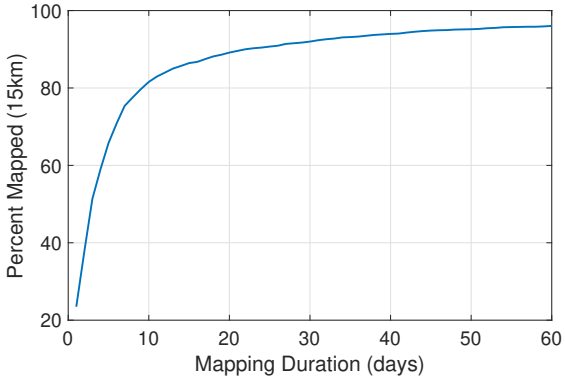

Figure 20: Percent of debris objects mapped (out of 2,311 total) from 400-500km altitude considering a fleet of 100 mapping CubeSats, as a function of mapping duration, assuming debris is detected if it masses within 15km of a CubeSat.

20% of the debris mapped in the first week. If the detection distance is decreased to 1km, the percentage of the debris mapped in one week decreases significantly (see Figure 21(b)). In one week, only about 1% of the debris is mapped even with 100 CubeSat fleet. However, in Figure 19, we see that approximately 8% of the debris is mapped with 100 CubeSats in 60 days.

3.3 Discussion

From Figure 20 and Figure 21, we see that the mapping rate (percent of debris mapped per day of mapping duration) is approximately linear when less than 70% of the debris population is mapped. Using this approximation and noting from Figure 19 that 8% of the debris is mapped in 60 days with 100 CubeSats (assuming a 1km detection distance), we estimate that it would take 525 days to map 70% of the debris with 100 CubeSats (assuming a 1km detection distance). The constraint that the majority of the debris in a 100km altitude ring be mapping in one year or less is not met with fewer than 100 CubeSats if the detection distance is 1km or less. However, if the detection distance is 15km, then (applying the same extrapolation to Figure 21(a), 70% of the debris could be mapped with 10 CubeSats in less than 1 month. From these results, it is clear that the detection distance more significantly influences the time required for mapping than the

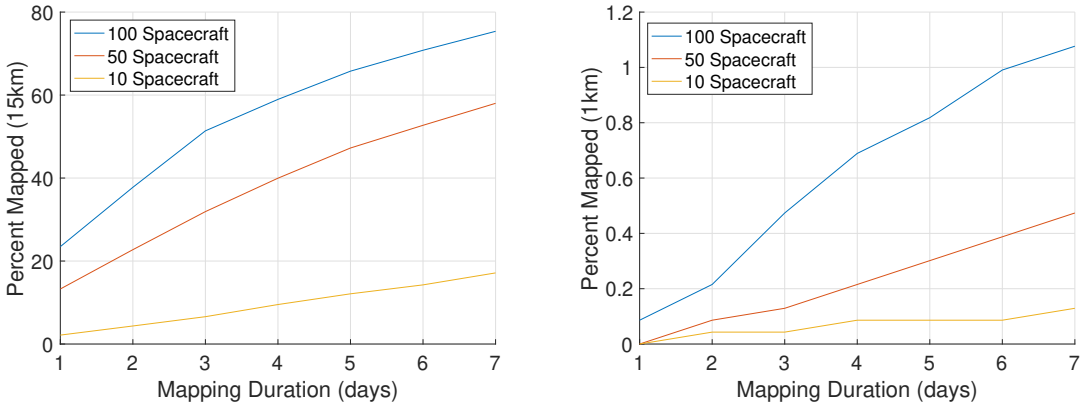

(a) 15km Detection Distance

(b) 1km Detection Distance

Figure 21: Effect of fleet size on time required to map debris. Note that the time required to map the debris does not scale linearly with the fleet size nor with the detection distance.

size of the constellation. The detection distance is critical to determining whether or not it is feasible to map orbital debris using a reasonably sized (< 100 vehicles) fleet of CubeSats.

Assuming a detection distance of 15km, and assuming that the time required to map the debris scales linearly with the area of the region to be mapped, we can approximate the time required to map debris at altitudes outside of the 400-500km range considered here. From Figure 20, we see that 80% of the debris is mapped in 10 days with 100 spacecraft and a 15km detection distance. Applying a linear scaling, we estimate that it would take approximately 11 days to map 80% of the debris in the 1200-1300km altitude range. The increase in time required to complete the mapping at 1200-1300km altitudes is small because the area to be mapped is only 11% larger than that of the 400-500km range.

The CubeSat orbits considered here are all equatorial. Since we know that all debris must pass through the equatorial plane, concentrating our CubeSats in the equatorial plane allows us to reduce the number of CubeSats required for mapping. Placing CubeSats on inclined orbits may be advantageous if there is some *a priori* knowledge of where debris may be concentrated (e.g. after an impact or explosion event) or if there is interest in assessing the safety of a specific orbit. Similarly, if a uniform distribution of debris is assumed, there is no particular advantage to adding maneuverability to the CubeSats unless there is a specific region of interest or a single CubeSat fleet is tasked to map debris in a series of altitude ranges.

Another option to consider in future studies is the possibility of using formation flight to aid in determining the direction of the debris motion. As discussed in Section 2, plasma solitons encode information about the debris size and speed. However, given a single soliton detection, the direction of the soliton's propagation (and the direction of the debris' velocity) is unknown. With two (or more) detections of the same soliton, it would be possible to calculate the direction of the soliton's propagation. Calculation of debris velocity from multiple detections would require fairly precise knowledge and control of the relative position of the two CubeSats. Future investigations should trade the value of directionality information with the increased complexity of the required CubeSat subsystems.

3.4 Summary

We have used the current population of detected orbital debris to approximate the undetected, sub-cm debris environment. We have simulated the time required to map the debris with ascending or descending nodes in the 400-500km altitude range using a fleet of equatorial CubeSats. The distance that a soliton can travel before dissipating is currently unknown, so we have left this as a variable in our simulation. We have considered CubeSat fleets of 10, 50, and 100 spacecraft. We see that with 100 spacecraft and a 15km detection distance, 80% of the debris can be mapped in 10 days. This duration is not expected to change significantly if a higher 100km ring of debris is considered. Ten days to map a population of debris is very short, indicating that it may be advantageous to either decrease the fleet size (to avoid the costs and risks

that come with a large fleet) or add maneuverability to the fleet. Adding maneuverability to the fleet will allow a mission architecture where a single 100km ring of debris is mapped over the course of 10 days and then the entire fleet maneuvers to higher altitude orbits to map another ring of debris. If the detection distance is small (1km or less), the time required to map the debris increases signficantly, with less than 10% of the debris mapped in two months with a 100 spacecraft fleet. The 18 months required to map the debris from 400-500km altitude (using 100 CubeSats with a 1km detection distance) is comparable to the duration of the witness plate methods (e.g., the LDEF was on orbit for 5 years[58]) used to date. Due to the potential hazard caused by the 100 CubeSats in orbit, the soliton detection of orbital debris is not beneficial in a mapping capacity if the detection distance is 1km or less, unless directionality of debris motion can be extracted from the signal.

4 CubeSat Design

We have previously discussed the characteristics of the solitons that are predicted to be generated by sub-cm orbital debris. There are several possible architectures for mapping the debris via soliton detection. In Section 3, we described the time and number of spacecraft required to map the orbital debris in a given altitude range. We have assumed that solitons produced by small orbital debris can be detected using identical CubeSats. The CubeSat platform is selected because these very small (typically less than 10x10x30cm and less than $\sim$ 5 kg) platforms can be inexpensively built and launched. In this section, we provide a preliminary design for a CubeSat to detect solitons produced by orbital debris. It is assumed that the solitons can be detected using a Langmuir probe and a Floating Potential Probe, which are the sole payloads of the CubeSat. In Section 5, we will discuss the design and limitations of a Langmuir probe for soliton detection.

In designing the CubeSat, the goal was to use as many commercial, off-the-shelf (COTS) parts as possible. Many of these parts have flight heritage and histories of success in prior CubeSat missions. If a 100+ CubeSat fleet was eventually planned to map small orbital debris, it might be cost effective to design some parts in-house, to remove unneeded functionality. However, the COTS-based design provided here provides a preliminary design to demonstrate the feasibility of hosting a Langmuir probe on a CubeSat for the purpose of detecting solitons. This design references documented CubeSat missions that also hosted Langmuir probes payloads, such as DICE (1.5U) and PIC.A.S.S.O. (3U) [12, 59]. Other CubeSats (e.g., BeEagleSat, TSat3, and Pegasus) have flown Langmuir probes on 2U platforms, but are less well documented in the literature. More recently Ex-Alta 1 (3U) and Hoopoe (2U) have flown as part of the QB50 project [60]. Other CubeSat's that did not carry Langmuir probes also influenced the proposed design, such as the Delfi Triple CubeSat NeXt whose design influenced the micro-controller and corresponding flight-board.

4.1 Communications

4.1.1 Radio Frequency Selection

The communication subsystem of the CubeSat will relay Langmuir probe data and floating potential probe data to a designated ground station. By relaying this information on each orbital pass of the ground station, large on-board data storage is unnecessary. We assume that the CubeSats are in circular equatorial orbits with altitudes ranging from 700 to 1200 km. The communications system is comprised of an on-board dipole antenna and an Ultra High Frequency (UHF) transceiver. These devices transmit the estimated 2 Gb of data gathered per day (see Section 5.4) by the dual probe system to available ground stations.

The radio frequencies that will be used range from 432 MHz to 470 MHz. This range encompasses two regions of the satellite radio frequency spectrum that apply to our CubeSat mission: the amateur satellite radio frequency from 432 MHz to 438 MHz, and the meteorological and environmental satellite band frequency ranging from 460 MHz to 470 MHz. These spectra are compatible with the chosen COTS antennae and radios. Ground stations are commonly assembled with COTS components at universities. Licensing and regulatory requirements also must be met for communications.

4.1.2 Radio Transceiver Selection

The desired radio must have low power requirements, perform in the proper radio frequency range, and possess a downlink rate greater than the total data collection rate to limit on-board storage requirements. The chosen transceiver is the Space Dynamics Laboratory Cadet U UHF radio. This 69x74x13mm, 200g radio fits all previously mentioned requirements, including size constraints and mass constraints [61]. This radio has flight heritage on-board the previously successful DICE CubeSat mission in 2011 [12], where it successfully transmitted Langmuir Probe data for over three years. With a maximum downlink rate of 3 Mbps and an uplink rate of 9.6 kbps, both within the range of UHF required, the radio was estimated to have the potential to rapidly transmit a full day's worth of probe data within the available contact time. A detailed link budget analysis was performed (see Table 8), assuming the ground station used a commonly-available tracking CubeSat tracking receiver with a 15.5 dB gain for the UHF signal. For the 700 km orbit, the downlink varied from 1.19 Mbps at zenith to a minimum of 62 kbps at the horizon, or a more conservative 156 kbps assuming the limiting contact is at 10° above the horizon. In either case, the selected radio would provide over 4 Gb of downlink over 15 daily overhead passes of an equatorial ground station by the equatorial satellites. At a 1200 km orbital altitude, the maximum data rate drops to 405 kbps, and the ground passes only occur 13 times per day, but the system still provides up to 2.4 Gb total downlink at a constant 3 dB link margin.

The Cadet U radio acts within the power constraints of the satellite's chosen batteries and solar panels, which are detailed in Section 4.4. A potential benefit to the use of the Cadet U radio is its storage system. Though we do not plan to store data after down-linking, should the need arise to hold off down-linking data to a later time, the Cadet U radio comes equipped with a 32 GB memory buffer. The Cadet U requires 0.3W of power while receiving data and 12W of power while transmitting data. Despite the apparent large transmission power requirement, this radio is ideal for our CubeSat because the majority of its orbit will be spent collecting data. In the worst case, 18.2% of the time on orbit will be required for transmission of the data. When not transmitting data, the communications subsystem will be in a listening mode for instructions from the ground station, as necessary.

Table 8: Link Budget

Data Type	Data Amount (bits/sec)
Langmuir Probe Data	11600
Floating Potential Probe Data	11600
Housekeeping Data	50
Error Margin	20%
Total	27900

4.1.3 Antenna Selection

An appropriate antenna for the transmission of Langmuir data on this CubeSat must have low power and volume requirements, as well as operate at the correct frequencies, and, preferably, be inexpensive. "Common choices for CubeSat antennas are monopole/dipole and patch antennas, which are both commercially available" [62]. The selected antenna system for our device is the Innovative Solutions in Space (ISIS) Dipole antenna system [63].

A dipole antenna is one of the simplest types of antenna, consisting of a divided metal rod split by an insulator, with a length of half that of the wavelength of the maximum desired radio frequency. In the case of our CubeSat, at a minimum frequency of 470 MHz, the antennae must be at least 33cm in length. The ISIS Dipole antenna system consists of 55cm length antennae, operating within the Ultra High and Very High Frequency ranges which encompasses the region of the radio frequency spectrum from 30 Mhz to 3 GHz. It is important to note that, due to the length of these antennas conflicting with initial size constraint of the CubeSat launch, these antennae must be deployed after launch, according to deployment regulations laid out in The CubeSat Program's design requirements [64]. According to Innovative Solutions in Space, this particular system has flight heritage since 2010. This dipole antenna system works in conjunction with the selected ISIS 2U Chassis, as the the chassis is specifically designed to house ISIS-built deployable antenna

systems. The antenna system's nominal power consumption would be less than 40mW and the system has a mass of less than 100g. CAD of the stowed antenna is shown in Figure 22.

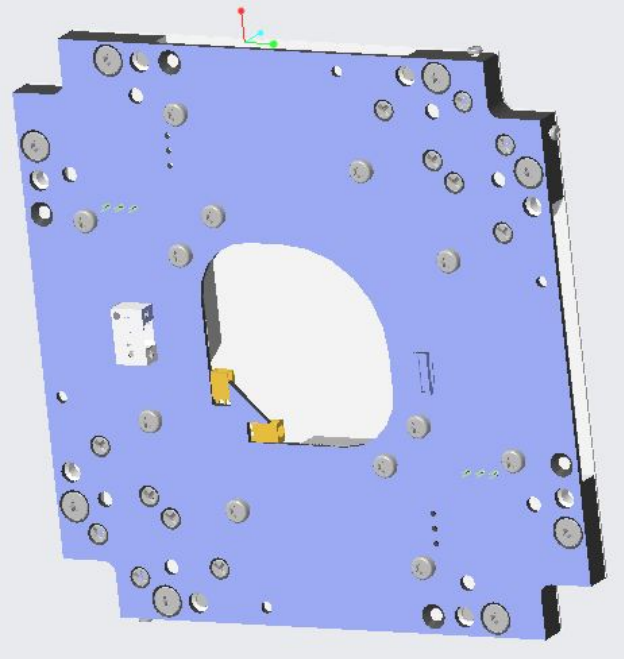

Figure 22: Stowed Antenna Configuration [63]. Note the long dimension of this antenna is 10cm.

4.2 Command and Data Handling System

The command and data handling system directs all processes carried out by the CubeSat after launch. The On-Board Computer (OBC) must interface with the Attitude Determination and Control Subsystem (ADCS), collect housekeeping data on the CubeSat subsystems (e.g., temperatures and voltages), receive and store science data and coordinate data downlink. We have chosen the ISIS On-Board Computer [65]. The command and control of the Langmuir and floating point probe will be completed by a separate science board, while data storage will occur on the OBC. The ISIS OBC has two slots for SD cards, and supports up to 32GB per slot, which is more than adequate to accommodate our anticipated production of 2.4Gb per day. As this OBC is probably overly capable for the needs of this mission, subsequent designs of this CubeSat should evaluate the benefits of using a custom, in-house CDH board.

4.3 Attitude Determination and Control System

The Attitude Determination and Control Subsystem (ADCS) controls the orientation of the CubeSat. There are two main requirements that drive the design of our ADCS: 1. the Langmuir probe and floating potential probe must be aligned perpendicular to the CubeSat's velocity vector, and 2. the solar panels must track the sun. The probes must be perpendicular to the velocity direction in order to avoid contaminating the plasma measurement by either increasing the ram current to the probe (in the case that the probe is 'in front of' the spacecraft) or pointing the probe into the spacecraft plasma wake. Additionally, by orienting the spacecraft perpendicular to the velocity direction, the ram area of the spacecraft is maximized, thus increasing the flux of ions to the spacecraft, which is necessary in order to ensure that the electric potential of the spacecraft does not vary, which would also contaminate the Langmuir probe results (additional detail in Section 5). Secondly, as is discussed in Section 4.4, this CubeSat will have two deployable solar panels, which must be sun-facing during the lit portion of the spacecraft's orbit in order to power the science payload and charge the batteries. We will be using a Dual UHF Dipole (DDUU) antenna system [66]. A dipole antenna

has a region where the signal generated from the source is omni-directional, and, thus, it does not impose strong pointing requirements on the spacecraft.

Because of the need to track the sun with the deployed solar panels, an active, three-axis stabilized ADCS is required. We have selected the MAI-400, which is a 1/2U ADCS unit containing three reaction wheels and compatibility with sun sensors [67]. The MAI-400 also has magnetotorquers, Earth-Horizon sensors and an integrated computer. Six sun sensors (also provided by MAI [68]) will be mounted on the exterior of the CubeSat and will be provide input to the control of the reaction wheels to ensure the desired attitude.

4.4 Electrical Power System

The power system design for CubeSats is particularly challenging due to the small surface area that the satellite provides for solar panels. Table 9 shows the power needed per orbit given the duty cycle of each component listed. Duty cycle is the percentage of the orbit that the component will need power during the mission. Most of the components will be working during the whole mission except the radio, which is typically transmitting for 20% of the orbit. Also, the power margin of 30% accounts for the inaccuracy of the power budget estimates.

Table 9: Power Budget Table [66, 67, 69, 70, 61, 12, 65]. The table has three columns of power use metrics and seven rows of spacecraft components, plus two summary rows.

Component	Power (W)	Duty Cycle (%)	Power Required Per Orbit (W)
Science Board	0.5	100	0.5
Dipole Antenna	0.04	100	0.04
UHF Radio (transmit)	12	20	2.4
UHF Radio (receive)	0.3	80	0.24
ADACS (avg)	1.33	100	1.33
On-Board Computer	0.55	100	0.55
Power System Electronics	0.015	100	0.015
		Power Margin	30%
		Total	6.4

4.4.1 Design and Components

Overall, the CubeSat needs about 6.4 W continuously over the orbit. Orbital periods will range from 98.8 minutes at 700 km altitude to 109.4 min at 1200 km. Using the 1200 km orbit as the worst case, and assuming that a ground station pass of 19.9 min duration happens within the 35 minutes of darkness, the total required energy storage for the night pass would be 1.85 Whrs for everything except the radio, 5.2 Whrs for the radio transissions, and 0.1 Whrs for the radio when receiving only, for a total energy storage requirement of 7.1 Whrs. We have selected the Crystalspace P1U power supply, which provides 22Wh and can receive up to 10W of solar input throughout its orbit. The power supply has dimensions of 96mm x 90mm x 13mm and mass of 140g [70].

During the 74.4 min of daytime in a 1200 km orbit, the power system has to supply an average of 6.4 W continuously to the spacecraft for operating power while also producing sufficient excess power to charge the batteries. Since the battery will have to supplement the live photovoltaic power to run the transmitter during the day, which could be as much as 20% of the time, we will allot 3 Whrs of battery energy storage to cover that portion of battery demand, which brings the total battery energy per orbit to 10.1 Whrs. Assuming an 80% charging efficiency, the spacecraft will have to generate that much energy during each daylight period, or an additional 8.1 W of power over and above spacecraft operating requirements. In all, the photovoltaic array needs to generate 15.1 W.

The selected solar panel is the solar panel DHV-CS-10 photovoltaic array, which has dimensions of 82.5mm x 98mm x 2.4mm and a mass of 50g [71]. Each module can produce 2.5 W of power when illuminated; this design requires six 1U panels deployed to face the sun continuously to provide sufficient power to operate the spacecraft throughout the orbit. In order to achieve 6U of solar panels facing the sun, there will be two deployable solar panels mounted on either side of the spacecraft. These solar panels will be deployed at 90°

to the CubeSat bus, so that they form a 20cm x 30cm planar face. An active attitude control system will ensure that this side is continually sun-facing.

4.5 Thermal System

Looking at the selected components of this CubeSat design, some components have integrated thermal regulation systems. For instance, the ISIS dipole antenna system has a thermal knife composed of wires that heat the antennas [63]. However, a thermal blanket for the CubeSat should be considered. Additional modeling is required to ensure that the additional structures are not necessary to maintain a safe operating temperature for the CubeSat components. Given that the current design is under the mass limit for a 2U vehicle (see Table 10), we are confident that any required passive thermal control system could be accommodated within the mass constraints of the 2U vehicle.

4.6 Structures

The design considerations for this CubeSat are intended to conform to those restrictions established by California Polytechnic University and The CubeSat Project. These constraints create a uniform platform in which universities and organizations can produce low-cost scientific experiments for space [64]. Each 1U (one unit) of a CubeSat is typically less than 1.33kg. Each 2U satellite has dimensions of 10 x 10 x 22.7cm. No part of the CubeSat may protrude from the constrained volume prior to launch. Any deployable must be stowed at the time of launch and may not be deployed until a set time after release from the deployment system. All electronics must be powered off before and during launch of the satellite. Along with these, the structure of the CubeSat is to be made of Aluminum 7075 or a material with a relatively similar thermal expansion rate [64].

The final structure of our soliton-detecting CubeSat is heavily dependent on the volume and mass of the COTS parts that make up all of the subsystems. The mass budget can be found in Table 10. Similarly, the volume budget can be found in Table 11. The mass of the deployable solar panel structure (not including the panels themselves) is estimated to be 100g, as it is likely to be less than half the mass of the full 2U chassis (206g). The DICE CubeSat hosted its Langmuir probes on scissor booms, each with a mass of 42g [12], thus we estimate the total mass of the probe booms to be 100g.

Table 10: Mass Budget [66, 70, 61, 71, 72, 73, 65, 68, 12]. The table has one column of masses and eleven rows of spacecraft components, plus two summary rows.

Component	Mass (g)
Langmuir Probes and Booms (est)	100
Dipole Antenna	100
UHF Radio	200
On-Board Computer	100
Science Board	45
Power System Electronics	140
Solar Panels	400
Deployable Solar Panel Structures (est)	100
Sun Sensors (3.5gx6)	21
ADACS	694
2U Chassis	206
Mass Margin	20%
Total	2527

An isometric view of the deployed CubeSat can be seen in Figure 23. Figure 24 shows a side view the CubeSat.

Our selected 2U chassis was developed by Innovative Solutions in Space (ISIS) and can be found at `https://www.isispace.nl/product/2-unit-cubesat-structure/`. It possesses flight heritage since 2013. This chassis is specifically designed to accommodate the selected antenna system, as the structure can be altered to allow easy deployment of the antennae once the satellite has reached orbit.

Table 11: Volume Budget [66, 70, 61, 71, 72, 73, 65, 68, 12]. The table has two columns of dimensions and volumes and ten rows of spacecraft components, plus two summary rows.

Component	Dimensions (cm)	Volume (cm^3)
Dipole Antenna (Stowed)	9.8 x 9.8 x 0.7	67.22
UHF Radio	6.9 x 7.4 x 1.4	81.7
Sun Sensors (each)	2.8 x 1.7 x 0.2	0.95
ADACS	10 x 10 x 5.16	516
On-Board Computer	9.6 x 9.0 x 1.2	103.7
Science Board	9.6x9.1x1.1	95
Battery	9.6 x 9.0 1.3	112.3
2U Chassis External Dimensions	10 x 10 x 22.7	2270
2U Chassis Internal Dimensions	9.84 x 9.84 x 19.7	1906
Science Booms (Stowed, each, estimate)	5 x 5 x 4	200
Total Utilized Internal Volume	-	1382
Remaining Internal Volume	-	524

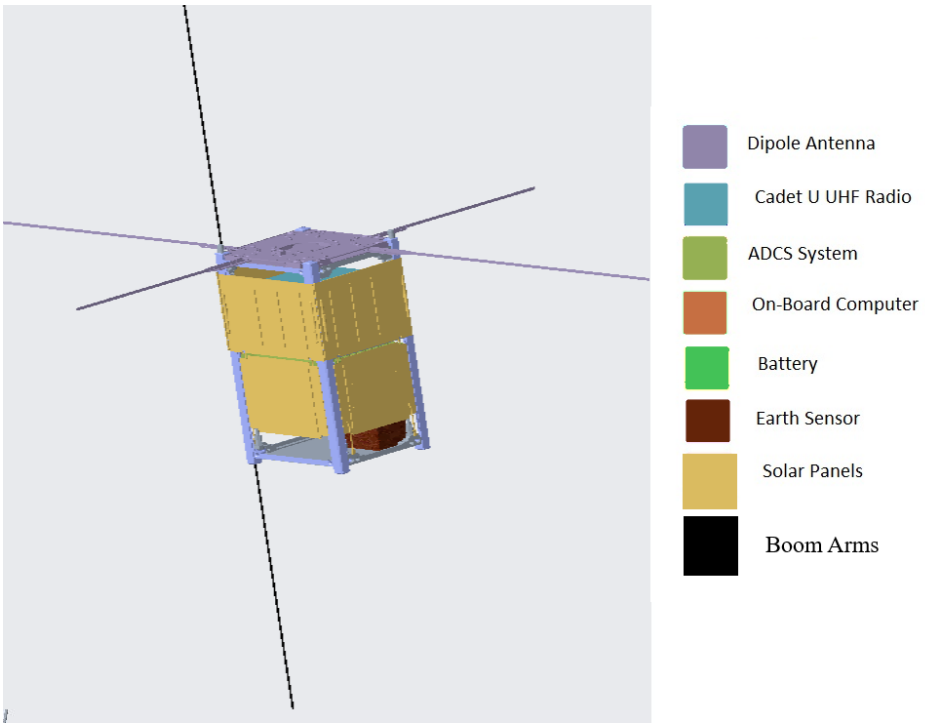

Figure 23: CubeSat Isometric View. The Langmuir and Floating Potential Probe extend axially from the ends of the 2U CubeSat. The antennas extend perpendicular to the probes from the top end of the CubeSat.

4.6.1 Deployable Booms

As will be discussed further in Section 5, in order to improve the accuracy of the Langmuir probe measurements, the CubeSat must also host a floating potential probe. As seen on other Langmuir probe-hosting CubeSats such as DICE and PICASSO, these two probes must be 30cm from the CubeSat bus in order to measure the freestream plasma environment (outside of the sheath generated by the charged CubeSat). Thus, these two probes must be on deployable booms.

The two individual boom holding either the Langmuir probe or floating potential probe will be situated on opposite ends of the satellite. This orientation maximizes the distance between the probes and ensures that neither of the probes are oriented in the ram direction or the plasma wake behind the CubeSat. Prior

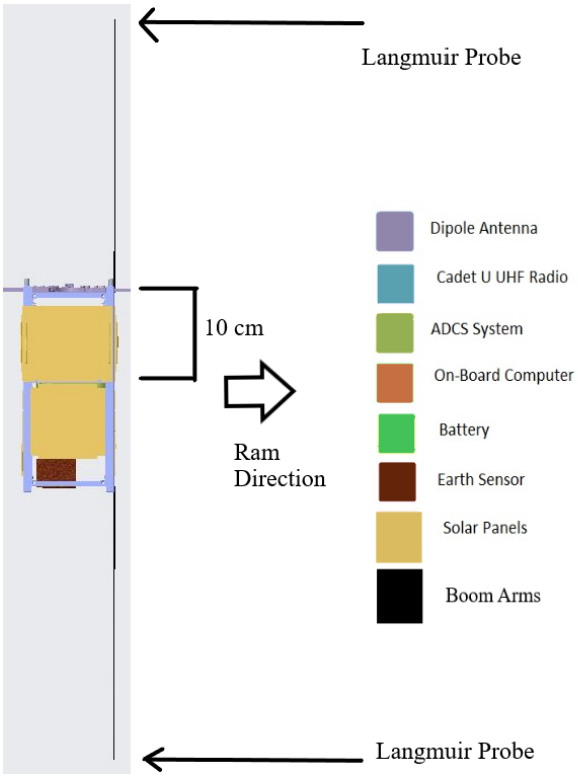

Figure 24: CubeSat Side View. The diagram shows that the spacecraft will be oriented so that probes are aligned perpendicular to the spacecraft velocity direction.

modeling has shown the necessity of lengthly booms as well as controlled spacecraft attitudes [74]. Through the use of our Attitude Determination and Control System (ADCS), when the two probes are deployed they will remain perpendicular to the ram direction for the duration of the orbit. The DICE CubeSat hosted its Langmuir probes on 13cm long scissor booms [12]. Future work should evaluate whether scissor booms are feasible for a 30cm length, or if an alternate design (e.g., an antenna-type boom as discussed in [72]) should be considered. The reliability of the deployment mechanism must be considered for alternate designs. The dimensions of the booms shown in Table 11 are estimated based on the DICE booms' design [12]. Note also that the booms must be electrically isolated from the CubeSat and probes to avoid influencing the plasma environment.

4.7 End of Life Disposal

The Inter-Agency Space Debris Coordination Committee recommends a maximum lifetime of 25 years for all Low Earth Orbiting (LEO) spacecraft [75]. Unfortunately, it is estimated that many existing CubeSat missions will violate this requirement given that most CubeSats lack propulsion systems and may lie in orbits minimally affected by atmospheric drag. It is well-known that spacecraft with mean-altitude of 700 km or less will naturally re-enter due to atmospheric drag within the 25-year period [76]. Additionally, the use of drag-balloons has been shown to extend the maximum mean-altitude for natural orbit-decay to 900 km [77]. The Aerospace Corporation has previously demonstrated CubeSat-based balloon technology with the AeroCube missions [77]. AeroCube 3 contained a 0.6 m diameter (inflated) deployable balloon, with a subsystem mass of 117g and a subsystem volume of 155 cm^3 [77]. At altitudes above 900 km, propulsive maneuvers are required to lower the orbit to within the drag-influenced region.

Given its mass and volume requirements, the AeroCube 3 balloon system could be accommodated by our 2U CubeSat, allowing deorbit from altitudes as large as 900km. However, deorbit from higher altitudes requires a propulsive maneuver. We calculate the ΔV required to transfer from a given altitude to either

700 or 900km altitude, where drag or a balloon system (at 900km) could subsequently deorbit the CubeSat. Figure 25 shows the Hohmann transfer ΔV's compared to the max ΔV for various off-the-shelf CubeSat propulsion systems, assuming a 4kg wet mass. This study indicates that a 4 kg CubeSat could de-orbit to the drag-influenced region from an altitude just under 1900 km using the MPS-120XL propulsion system. Additionally, if a drag balloon is employed and the target final orbit altitude is 900 km, the maximum altitude increases to 2100 km.

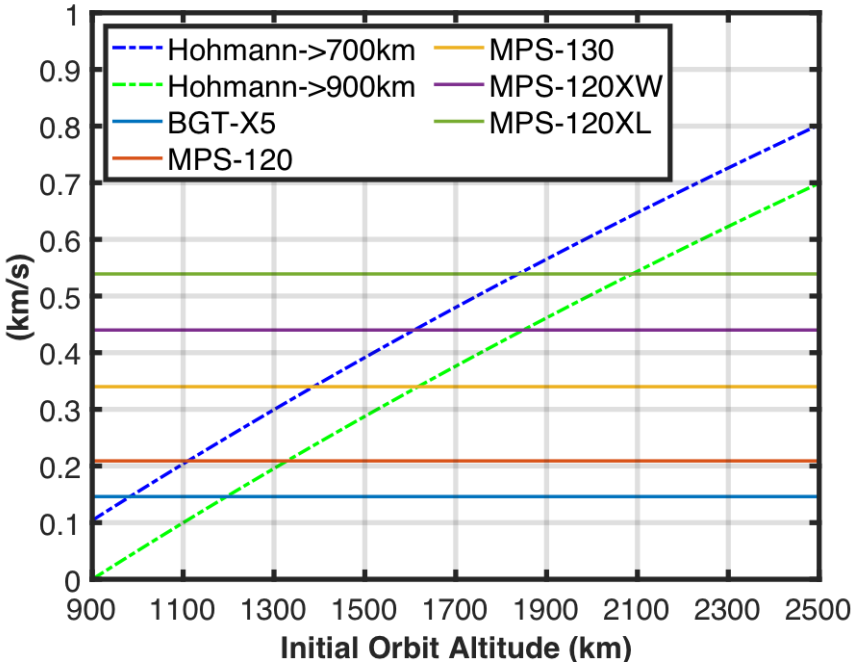

Figure 25: Hohmann transfer ΔV requirements for various initial orbit altitudes and maximum ΔV for off-the-shelf propulsion systems. Note that this analysis assumes a 4kg spacecraft. The BGT-X5, MPS-120, and MPS-130 thrusters require 1U of volume, and the MPS-120XW and MPS-120XL are 1U x 2U in size [78, 79]. The MPS-120XL could deorbit the example CubeSat to 700km altitude via a Hohmann transfer from an initial 1800km orbit. Similarly, the CubeSat could be deorbited from 2100km altitude to a 900km orbit with theMPS-120XL. The other thrusters can deorbit from lower initial altitudes.

If soliton detection is desired at altitudes above 700km, an active deorbit strategy must be employed. From 700-900km in altitude, a balloon-assisted deorbit is likely possible within the constraints of our 2U vehicle. If debris mapping occurs at altitudes above 900km, then a propulsive deorbit scheme is required, and the spacecraft will need to grow in size to at least 3U. To deorbit from a 2100km altitude orbit, the MPS-120XL propulsion system is required, which would require at least a 4U CubeSat, which would probably necessitate transitioning to the commonly used 6U form factor.

4.8 6U Form Factor

As mentioned previously, in order to enable mapping at and deorbit from higher altitudes, at least 2U of fuel is required. This preliminary design has shown that the payload for a mapping CubeSat could be accommodated in a 2U form factor. However, if additional fuel necessitates the transition to a 6U form-factor, then the design of other subsystems is simplified. Because 6U of solar panels are required to execute the science and housekeeping functions, a 6U CubeSat would not require deployable solar panels, and could instead just use body mounted panels. This would simplify the structural design of the CubeSat and potentially loosen spacecraft pointing requirements. Additionally, a 6U spacecraft would also have approximately 2U available for fuel for maneuvers (in addition to the deorbit maneuver). This would allow a

single CubeSat to maneuver to and map debris at multiple altitude bands. Future studies should investigate the trade-off between CubeSat size and increased maneuverability.

4.9 Summary

Langmuir probes have previously been flown on Earth-orbiting, 2U CubeSats. We have presented a preliminary CubeSat subsystem-level design based on COTS components. In this design and the 2U form factor, there is mass, volume and power margin. The spacecraft's attitude will be controlled using sun sensors and reaction wheels so that the deployed solar panels and a body-mounted solar panel track the sun. The Langmuir and floating potential probes will be mounted on 30cm deployable booms and will be deployed perpendicular to the ram direction to limit contamination of the signal by the CubeSat bus. Amateur or meteorological communication frequencies would be used along with a dipole antenna. There is sufficient mass margin to account for wiring mass, as well as accommodate any additional structures that may be required for thermal control. Natural deorbit is feasible for altitudes below 700 km. Deorbit using an inflatable balloon is likely possible within the 2U form factor at altitudes up to 900km. At altitudes larger than 900km, the propulsion required for deorbit necessitates a larger form factor, at which point a 6U, maneuverable CubeSat may be advantageous.

5 Soliton Detection

In our system, the estimated maximum Debye length is 15cm. The boom length should be roughly twice the Debye length to ensure that measurements are being taken outside of the CubeSat sheath [80]. Thus, both the Langmuir Probe and the Floating Potential Probe will both be placed on deployable boom arms 30cm in length.

The sole mission for our CubeSat is to detect plasma solitons produced by sub-cm orbital debris. The baseline payload to detect these plasma solitons is a Langmuir probe. The Langmuir probe is a simple and inexpensive instrument for plasma diagnostics for both laboratory and space plasmas. Historically, Langmuir probes have been implemented on sounding rockets and satellites to generate data on plasma conditions in space. By making *in situ* measurements, it is possible to obtain information on space plasma parameters such as plasma density and temperature. The soliton signal manifests in the plasma density. Thus, the Langmuir probe provides a mechanism to detect solitons.

We begin by providing a brief introduction on the basics of Langmuir probe theory to give some context to the Langmuir probe design process. Section 5.1 will also discuss the probe and boom geometry, explain the probe interface with the CubeSat, and discuss the power requirement calculations. Section 5.3 highlights some of the primary difficulties of Langmuir probe designs, specifically in relation to CubeSat platforms.

5.1 Langmuir Probe Design

5.1.1 Langmuir Probe Theory

A Langmuir probe is a metal collector inserted into a plasma to which a DC bias voltage is applied. Typical geometries for Langmuir probes are spherical, cylindrical, and planar. As the Langmuir probe sweeps through a range of voltages, the current between the Langmuir probe and the satellite's ground is measured. The measured current is then graphed against the applied bias voltage to create an I-V characteristic curve.

As the probe voltage increases positively relative to ground, electrons are increasingly attracted to the probe tip. This is called the electron saturation region. As the probe voltage decreases relative to ground, ions are attracted and electrons are increasingly repelled. This region is known is a the ion saturation region. The electron retardation region sits in between the two saturation regions, and is represented by the steep part of the curve. The plasma floating potential, V_f, is the equilibrium potential attained by a conductor immersed in a plasma environment such that there is no net current to the probe. The plasma potential, V_p, "is the potential at which no sheath effects are present between the probe and the surrounding plasma" [81].

There is no general theory of Langmuir probes that can be applied to all measurement scenarios because there is a dependence on probe geometry, plasma temperature, and other factors. There are two primary

theories that approximate plasma characteristics from Langmuir Probe measurements: 1) Orbital-Motion Limited (OML) and 2) Sheath Area Limited (SAL). The OML regime can be adopted if the radius of the probe, r_{lp}, is smaller than the Debye length (λ_D) [82]:

$$\lambda_D = (\frac{\epsilon_0 k_B T_e}{n_e q^2}) \tag{64}$$

where ϵ_0 is the permittivity of free space, k_B is the Boltzmann constant, T_e is the electron temperature, n_e is the electron density, and q is the elementary charge of an electron. We will focus on the OML theory because our probe tip will be much smaller than the Debye length, which ranges from 0.24-15cm for 400-1600km altitude above the Earth. Current in the electron saturation region in a non-drifting, collision-less, and unmagnetized plasma given by OML theory is generally described by [83]:

$$I_e = A n_e q \frac{2}{\sqrt{\pi}} \sqrt{\frac{k_B T_e}{2\pi m_e}} \sqrt{1 + \frac{qV}{k_B T_e}} \tag{65}$$

where A is the surface area of the probe, m_e is the electron mass, and V is probe potential with respect to the plasma.

The ion saturation current is described using a model developed by *Hoegy and Wharton* [84] to include spacecraft velocity with the probe axis perpendicular to the velocity vector [84]:

$$I_i = A q n_i v_i \frac{1}{\sqrt{\pi}} \sqrt{1 + \frac{k_b T_i}{m_i v_i^2} + \frac{2qV}{m_i v_i^2}} \tag{66}$$

where n_i is ion density, v_i is the ion velocity with respect to the spacecraft, T_i is the ion temperature, m_i is the mean ion mass of dominant ion species, and V is the probe voltage with respect to the plasma. This model attempts to explain ion current for more massive ions in the drifting Maxwellian, leading to the dominance of ion current in the ram direction of the probe [85]. The ion ram current contribution is represented by the first term under the radical. "In LEO, this term can outweigh the other two terms by an order of magnitude, contributing almost the entire current in the ion saturation region" [86]. The second term represents the ion current collected by the ion thermal velocity, and the third term represents the ion current collected due to the electric field generated by the Langmuir probe [83].

It is possible to obtain the electron density by measuring the current to the probe at multiple voltages [87]:

$$\Delta I_e^2 = \frac{2q}{m_e \pi^2} (A n_e q)^2 \Delta V \tag{67}$$

where ΔV is the difference in voltage. Eqn 67 can be solved for n_e and holds true only for cylindrical Langmuir probe geometries.

5.1.2 Instrument Geometry

The chosen geometry for the Langmuir probe instruments for this mission is cylindrical. A cylindrical geometry was selected for several reasons. The altitude range for this mission is between 400km to 1600km. In this region, the expected Debye length, which can be seen in Table 12, can be as large as 15cm. Therefore, the sweeping Langmuir probe will be operating under the OML condition, such that the radius of the Langmuir probe, r_{lp}, is less than the Debye length. Adopting a cylindrical geometry allows the radius of the probe to be sufficiently small while the length can be long so as to increase the surface area of the collector. This will ensure that the probe will draw acceptable current even at low electron densities [88]. The minimum anticipated Debye length is 0.24cm at 400km altitude, so the radius of the Langmuir probe was chosen as 0.20cm to ensure that the OML regime is always satisfied even at lower altitudes.

The length of the collector was determined to be 5cm from literature review, which found typical collector lengths of 5-10cm with similar expected plasma densities [72]. Additionally, the length selection of 5cm for the probe was justified using Eqn 66. To find the necessary length, a minimum current of 1×10^{-9} A was used in the calculation. The minimum current was chosen because of device limitations shown from previous Langmuir probe ionospheric measurements [72]. The ion saturation current was used to solve for

Table 12: Expected plasma parameters for the minimum and maximum spacecraft altitudes considered. Parameters vary depending on solar activity, illumination, altitude, and latitude. [89, 90, 82]

	400km	1600km
Electron Density n_e (m^{-3})	10^8	10^{12}
Electron Temperature T_e (K)	1100	5500
Debye Length λ_D (m)	2.4e-4	0.154

collector length because the ion current is expected to be the lowest magnitude of current collected. Several assumptions were made to simplify the model: at higher altitude ranges (> 75km), $n_i \approx n_e$ [82], and $v_i \approx$ spacecraft velocity. This is a reasonable approximation because the ion saturation current will be primarily attributed to ram side ions. Using Eqn 66, and our chosen probe geometry, we found that the amount of ion current collected varies greatly depending on ion density, from 10^{-12} to 10^{-8} A. Therefore, ion current can only be reliably collected at higher plasma densities ($> 10^9$ m^{-3}). This finding is consistent with other works that calculated collector length using similar assumptions [86]. Table 13, based on [86], shows the results of our calculations.

Table 13: Cylindrical probe size necessary to achieve a minimum of $1x10^{-9}$ A of current with stated assumptions. Assuming a probe length of 5cm, reliable current measurements are only possible in regions where the ionospheric density is greater than 10^9 m^{-3}. This table has three columns and three rows, showing how the required probe characteristics change with the ion density.

Ion Density (m^{-3})	Probe Area (cm^2)	Probe Length (cm)
10^8	73.81	117.5
10^9	7.381	11.75
10^{10}	0.7381	1.175

One of the two Langmuir probes on this mission will be a Floating Potential Probe. A Floating Potential Probe (FPP) is a Langmuir probe instrument that is designed to measure the floating potential. "Simply stated, the FPP is a very high precision volt meter that measures the potential difference between two conducting surfaces" [91]. The use of a FPP is necessary to account for the charging of the CubeSat chassis, which is discussed more in Section 5.3.1. A FPP has been previously implemented on the International Space Station, which found that, "all three Langmuir probe instruments (Floating Potential Probe, Wide Langmuir Probe, and Narrow Langmuir Probe) provide the ISS floating potential value to within ±2 volts of each other" [92]. Alternatively, an emissive probe can be used to determine the floating potential by plotting the probe bias at the floating condition against the probe temperature [93].

5.1.3 CubeSat Mounting

The two cylindrical Langmuir probes will be mounted along the long axis, on the top and bottom faces of the CubeSat, perpendicular to the velocity vector. The probes will be mounted along the long axis to acquire measurements in undisturbed plasma flows so to minimize disturbances from sources such as the plasma wake of the CubeSat [94]. It has been shown through simulations of a 1.5U CubeSat that plasma density in a CubeSat wake can create a region of ion focusing [74]. It is important for our mission to avoid such fluctuations in plasma density readings so that we can attribute perturbations in density measurements to solitons.

A perpendicular probe orientation is also important to ensure that enough ion current is collected. It has been shown experimentally that a perpendicular facing cylindrical probe collects a significantly larger amount of ions when compared to a parallel cylindrical probe [95]. The higher amount of ion collection was attributed to the larger cross-section in the ion flow. Furthermore, our calculations for probe collector length were conducted using Eqn 66 which assumes that probes are oriented perpendicular to the plasma flow. A ±10° angle from the perpendicular direction is calculated to have a 1.6% decrease in ram collection area [96]. Thus, ±10° deviations from the desired attitude should not significantly effect the spacecraft potential.

The probes will be deployed on the ends of 30cm long cylindrical booms. The booms should be made of an insulated material [12], and can be manufactured from composite carbon fiber tubes which is non-conductive [72]. The boom length was chosen to be 2 times the maximum expected Debye length of 15cm. As the CubeSat becomes progressively charged, a sheath forms around the spacecraft that extends a few Debye lengths out from the satellite surface [80]. A boom length of 30cm or greater guarantees that measurements are made in the undisturbed plasma outside of the sheath [88]. It is important to take measurements outside of the sheath because the plasma densities observed inside a plasma sheath will be different than the freestream densities, and measurements made within the sheath could deviate from OML theory [97].

5.1.4 Power Requirements

To get an estimate of the power requirements for the Langmuir probe instrument, information from previous ionospheric Langmuir probes was sought. Unfortunately, most previous works excluded power considerations for the probes from their design reports. Nominal power consumption was found for entire science subsystems, which included Langmuir probes with other instruments, to be < 2W in a worst case scenario [96]. The CubeSat mission DICE, which hosted spherical Langmuir probes on a 1.5U CubeSat, was capable of maintaining a power consumption of 411.4mW for their entire science board, which hosted 2 Langmuir probes, 4 Electrical Field probes, 1 Floating Potential probe, and a science magnetometer [12].

5.2 Probe Operations

Due to the complexity of making Langmuir probe measurements using a CubeSat, numerical simulations (e.g. Particle in Cell (PIC) and Space Plasma Interaction Systems (SPIS)) should be completed. Through simulations and laboratory experiments, several CubeSats have used an operational sweep voltage ranging from -3V to +15V [87, 59]. The PIC.A.S.S.O. CubeSat probe design is intended for collecting measurements at much lower altitudes (the highest being 550km), however, their simulations account for electron temperature and density ranges similar to those expected for this mission, 600K to 6000K and $10 \times 10^8 \mathrm{m}^{-3}$ to $5 \times 10^{12} \mathrm{m}^{-3}$.

The PIC.A.S.S.O. PIC simulations [59] showed that, although probe voltages from -5V to 13V are commanded, the actual probe potentials are only -5V to 4V, due to the variation in the spacecraft floating potential. Moreover, their simulations indicated that spacecraft charging variation is more severe at higher electron densities, which corresponds to lower altitude ranges. A sufficiently large positive potential is required to fully characterize the electron saturation region. Therefore, we expand our a voltage sweep to -3V to +15V. Further examination of sweep voltage is required to satisfactorily explain the surface charging effects that will be experienced on this mission.

5.3 Limitations of Langmuir Probes

5.3.1 CubeSat Surface Charging

There are several limitations of hosting Langmuir probes aboard CubeSats. Perhaps the most problematic issue is that the CubeSat has a limited conductive surface area. Typically, the satellite bus acts as the reference ground for *in situ* plasma measurements. As the applied voltage bias to the probe is swept, the satellite bus must be able to draw a similar amount of current from the plasma to remain at a constant potential. This is more relevant as the probe is biased to greater positive potentials (causing the probe to attract electrons) because the satellite can only reliably collect ion current from ram ions. When the probe is biased negatively (so that the Langmuir probe attracts ions), the bus can collect electrons on all faces of the CubeSat, as less massive electrons are easily attracted to the CubeSat bus. If the CubeSat bus cannot draw enough current to balance the current collected by the probe, the satellite's electric potential will change. This will cause a drift of the probe's electrical ground [86, 12, 59]. This is of critical importance when designing a voltage sweep range for the Langmuir probe because if spacecraft potential becomes more negative than the upper bounds of the voltage sweep, then the electron saturation current measurements will not be gathered.

The issue of a drifting electrical ground is more significant for CubeSats than traditional spacecraft because the surface area of the CubeSat bus is limited. It has been shown experimentally that to avoid

significant drift in the reference potential, a ratio of 1000 or greater must be kept between the reference electrode surface area (i.e. the area of the ram satellite face, A_{sat}) and the probe collection surface area (A_{lp}) [98]. The probes presented in this paper are intended to be flown aboard a 2U CubeSat, which is characterized by dimensions of 10x10x22.7cm. Therefore, it is unrealistic to design for an area ratio of such a magnitude due to our size limitations. Realistically, the ram side collection area of our CubeSat is around 200 cm^2. However, a worst case scenario where half of one panel of the long axis will be conductive and available for ram ion collection is assumed. Therefore, the effective ion collection area is found to be $A_{sat} = 113.5$ cm^2. Given that the probe collector surface area is roughly 6.3 cm^2, the ratio of ion collecting surface area (A_{sat}/A_{lp}) ≈ 18, which is much lower than the suggested 1000. Previous CubeSat designs that have implemented Langmuir probes have acknowledged this issue. For example, The PIC.A.S.S.O. CubeSat that was to be launched in 2018 used a specific measurement technique that biased one probe to read current measurements, and used another probe to measure the floating potential [59]. By combining the measured floating potential with respect to the spacecraft along with the probe potential with respect to the spacecraft, the probe potential relative to the floating potential can be known [59]. An alternative method devised for controlling the surface charging is electron guns, which are capable of emitting 10 to 100 μA [81].

5.3.2 Contamination Effects

Among the factors that are influential in making accurate readings in ionospheric plasma, contamination (adsorption/deposition of ions) is one of the biggest issues. When a bias is swept on a contaminated probe in both directions, hysteresis is exhibited in the generated I-V curve. However, hysteresis has been shown to diminish in ionospheric plasma measurements at sampling frequencies of 10Hz or greater, as well as at lower plasma densities [87, 88]. Typical contamination cleaning systems involve large voltage sweep magnitudes of $\pm$100V or more, which is impractical for a CubeSat. Additionally, even more efficient methods of probe cleaning (e.g. heating of the probe) require relatively high amounts of power at $\approx$ 2W [99]. In order to minimize contamination effects, a sweep frequency of 10Hz will be implemented on the probe.

5.4 Data Volume

In order to calculate the volume of data produced by the Langmuir probe, we assume that both the Langmuir probe and FPP will complete 29 sweeps/sec, with one 'sweep' defined as data collection at 25 different probe voltages. 50 sweeps/sec has previously been baselined for the PIC.A.S.S.O. mission [59]. With 16 bits of data per voltage, this measurement frequency will produce 23,200 bits/sec. Assuming continuous operation, this will produce 2.4Gb/day.

5.5 Summary

The baseline payload for detecting plasma solitons is through the use of a Langmuir probe, in concert with a Floating Potential Probe. This two probe architecture has previously been discussed for the PIC.A.S.S.O. mission and implemented on the DICE mission. However, hosting a Langmuir probe on a CubeSat has the significant drawback that the floating potential of the CubeSat bus may vary during the potential sweep of the probe because the ram surface area of the bus may not be large enough to collect a sufficient ion current to negate the electron current collected by the Langmuir probe. In order to limit this effect, we have mounted the probes so that the long axis of the CubeSat will be in the ram direction. Nonetheless, additional investigation is required to ensure that the maximum and minimum bias voltages applied to the Langmuir probe are sufficient to collect the required plasma density measurements.

For our baseline payload, we will have a 5cm long, 0.2cm diameter cylindrical Langmuir probe mounted on a 30cm boom to ensure that the probe is outside of the CubeSat's plasma sheath. The Langmuir probe and floating potential probe package is estimated to require less than 400mW of power, based on the power consumption of the DICE mission [12]. Additionally, the planned voltage sweep on the Langmuir probe is from -3V to +15V. The probe will produce 2.1Gb of data per day.

6 Alternate Architectures

NIAC requires that all technologies be developed in a mission concept. The vast majority of this report has considered a mission concept where plasma solitons are detected by a fleet of equatorial CubeSats. However, there are several alternate mission concepts where soliton detection could be used to map sub-cm orbital debris, including ground-based methods and hosted payload sensors.

6.1 Ground Based Detection of Solitons

The properties of the ionospheric plasma are frequently measured using ground-based methods. Depending on the sensitivity of those methods and the size of the expected plasma solitons, it may be possible to detect the orbital debris signal from the ground. While it is unlikely that ground based detection methods would be suitable for mapping small orbital debris, this detection concept may provide a low-cost method to test our predictions of soliton characteristics and advance the TRL of this technology.

The primary ground based instruments for measuring ionospheric density are ionosondes and coherent and incoherent scatter radars. Ionosondes work on the principle that a radio wave will be reflected when the plasma frequency (which is proportional to the square root of the electron density) is equal to the frequency of the radio wave. As an example, the Lowell Digisonde can emit radio waves with 1kHz frequency resolution [100], which corresponds to a electron density measurement accuracy of approximately 300 m^{-3}. Referring to Figure 14, we see that the perturbed ion density in a soliton generated by sub-cm debris is approximately 2-3x the nominal density ($10^{11} m^{-3}$ for the High LEO 1 region). Thus, assuming that the plasma remains quasi-neutral in the soliton (i.e. the ion and electron densities are approximately equal), then the soliton amplitudes predicted in our work should be resolvable by ground-based ionosondes. However, ionosondes can only probe the ionosphere at altitudes below the peak ionosphere density, which occurs at altitudes between 200 and 400km [101].

Incoherent scatter radar (ISR) works off a similar concept, but instead of just measuring the time required between the transmission and reflection of the radio wave (which gives the altitude of reflection, ISR senses the strength of the returning echo signal to determine the density of the plasma electrons as a function of altitude. ISR can also measure the plasma temperature. EISCAT (the European Incoherent Scatter Scientific Association, which operates four radar antennas) is able measure plasma properties at altitudes up to 2000km, well within the range of altitudes where it is expected that solitons could be produced. However, many ISR facilities are located at high latitudes, where plasma densities are decreased and soliton generation becomes more difficult. While ISR has a higher spatial resolution than ionosondes, future work should investigate whether the small physical width (cm's) of the solitons is detectable from the EISCAT facilities.

6.2 Hosted Payload

In this study, we have considered soliton detection by a fleet of Langmuir-probe carrying CubeSats. However, an alternate architecture would be to have a small, data-light instrument package to detect solitons that could be hosted by other, larger Earth-orbiting spacecraft. The hosted payload model reduces the risk of adding to the orbital debris problem by eliminating the need for a fleet of 10's of CubeSats. Additionally, the soliton-sensing payload would be providing data that would be useful to the host spacecraft, and would likely have monetary value to the spacecraft operator. If every new vehicle in Earth orbit carried this payload package (making it like the Pitot Probe of LEO), a high resolution and accurate debris map could be quickly generated. A second major benefit of hosting a soliton sensor on a spacecraft with a different primary mission is that the host spacecraft will be larger than a CubeSat. As noted in Section 5, one of the main challenges associated with detecting plasma solitons using a Langmuir probe on a CubeSat is that the floating potential of the CubeSat is likely to vary due to the small ram cross section of the vehicle. As long as the ram side surface area of the spacecraft body is greater than or equal to 1000 times the surface area of the probe, the reference potential will not vary substantially. Thus, hosting a Langmuir probe on a larger spacecraft will simplify the measurement.

A soliton sensor payload would need impose limited mass, power, volume and pointing requirements on its host vehicle. A deployable boom system would be required to extend the probes outside of the sheath

region so that perturbations in measurement are minimized. A boom length of 30cm will achieve this for low Earth orbit measurements in many cases, but may need to be extended for larger expected Debye lengths. Additionally, probe geometry may also vary depending on the the Debye length, which is a function of altitude. Table 14 below details the necessary equipment for a Langmuir probe hosted payload. The estimates shown in the table can be considered minimum requirements needed for proper Langmuir probe operation. An electrometer is required to measure the current to the probe, but is usually an application-specific integrated circuit on the power board. For instance, DICE CubeSat used a single printed circuit board that housed all the science electronics [12]. The probes would need a data handling board, and a power board however, the probes may be able to use those of the host satellite. The boom deployment power found in Table 14 is estimated from [12].

Table 14: Requirements for a soliton-detecting Langmuir probe payload to be hosted by a full-sized LEO spacecraft. With a full-sized LEO host, the Floating Potential Probe will be unnecessary. From Table 8, the Langmuir probe will produce 13980 bits/sec that must be downlinked by the host spacecraft. Mass and volume estimates based on values provided by [12]. This table has three columns with the parameters of interest to a host spacecraft and three rows of payload components.

Component	Mass (g)	Volume (cm^3)	Power (W)
Langmuir Probe	4	(inc w/Boom)	(inc w/Science Board)
Boom	50	200 (stowed)	0.2 (during deployment)
Science Board	45	95	0.5

7 Conclusions and Future Directions

The goal of this report was to assess the feasibility of using a fleet of CubeSats to map sub-centimeter orbital debris in low Earth orbit by detecting precursor plasma solitons generated by the debris. To that end, we have modeled the solitons that would be produced by sub-cm orbital debris, in order to characterize the regions in which debris will produce precursor solitons as well as the amplitude and width of the solitons (which drives detectability). We have also simulated the time required to map debris in a 100km altitude ring as a function of the number of CubeSats deployed and the distance that a soliton can travel before dissipating. We have presented a preliminary design for a 2U CubeSat hosting a Langmuir probe and floating potential probe to detect the solitons. In this section, we will summarize the major results of this investigation and present the highest priority areas of follow-on work.

Sen *et al.* previously showed that charged debris moving through a plasma could be modeled using the forced KdV equation and would produce precursor solitons [2, 3, 4]. We have modeled the plasma signatures of debris from 1mm-1.25cm in size at a range of altitudes. We have develop equations that give the upper and lower limit of the debris velocity that will produce precursor solitons, which is critical to determining whether or not a given debris population can be detected using this method. Additionally, we see that at less dense plasmas (for example, in GEO or at polar latitudes), precursor solitons are extremely unlikely from debris of this size. We have shown that, at an altitude of 1200km, sub-cm debris generate precursor solitons that travel ahead of the debris. We have also shown that the density variations that compose the solitons are large, 2-3x the baseline plasma density and the solitons are typically several cm in width. This work represents a significant improvement in our understanding of the solitons that may be produced by small orbital debris and provides key parameters for future efforts to observe these features.

In assessing the feasibility of mapping sub-cm debris using a fleet of CubeSats, we considered two main requirements: 1. the debris should be mapped using 100 CubeSats or less to avoid increasing the congestion of the LEO environment, and 2. the debris in a 100km altitude ring should be mapped in one year or less, in order to represent a significant improvement on 'witness plate'-type mapping. To accomplish this, we considered a fleet of equatorial CubeSats with orbits ranging from 400-500km altitude. Our simulations showed that in two months it is possible to map more than 90% of the orbital debris in this band using a fleet of 100 CubeSats, if it is assumed that solitons can travel up to 15km without dissipation. Mapping duration and fleet size are sensitive to the detection distance (i.e., the distance that a soliton can travel before dissipating due to variations in the plasma environment). Even considering a detection distance of

5km, more than 70% of the debris in this ring could be mapped in two months with 100 CubeSats. However, if the detection distance is only 1km, then fewer than 10% of the debris would be mapped in two months with 100 CubeSats. We also explored the impact of fleet size. With a detection distance of 15km, 70% of the debris in this ring could be mapped in one month using only 10 CubeSats. The fleet size becomes more critical as the detection distance increases. We also extrapolated our results at 400-500km to other altitude rings and saw that mapping durations do not increase significantly when the 1200-1300km ring is considered.

In this study, we considered detecting solitons using Langmuir probes. Langmuir probes have previously been flown on CubeSat missions [12, 102, 59]. However, because of their small size, the electric potential of the CubeSat may vary during Langmuir probe measurement. In short, the current to the Langmuir probe from the plasma is recorded as the voltage on the probe is varied. Since the probe voltage is referenced to the electric potential of the CubeSat, if the electric potential of the CubeSat is time varying, then you don't know the voltage of the probe relative to the plasma. Prior work has used a floating potential probe (basically, a second Langmuir probe, but whose potential is not varied) to measure the variation in the electric potential of the CubeSat. Additionally, the Langmuir probe must be extended 30cm from the CubeSat bus and the CubeSat's attitude must be controlled so that probe is not in the plasma wake of the vehicle. We estimate that a single Langmuir probe (as could be hosted on a full-sized LEO spacecraft) would produce 1.2 Gb/day. For a CubeSat, which must also host a floating potential probe, the total data volume would be 2.4Gb/day.

We have designed a 2U CubeSat from commercial, off-the-shelf components that is capable of hosting the Langmuir probe and floating potential probe payload. This design includes two deployable solar panels and requires an active attitude control system in order to produce enough power to downlink the data at 700km altitude. At higher altitudes, it would not be possible to downlink the full data volume currently predicted. However, the data volume could be easily reduced by decreasing the frequency of the Langmuir probe sweeps.

There are three main priorities for future work: 1. predicting the dissipation of the solitons, 2. determining whether solitons could be observed from the ground as a proof of concept, and 3. conducting a system architecture trade. In our studies of the CubeSat fleet design, we saw that the time required to map a given 100km altitude ring is heavily dependent on the distance that solitons can travel before dissipating. Solitons will dissipate in the spatially varying plasma environment. Now that we are able to simulate the plasma solitons, our next step is to simulate their propagation through a varying plasma environment in order to determine their dissipation rate. Secondly, now that we have predictions of the characteristics of plasma solitons produced by orbital debris, it would be advantageous to be able to detect these signatures from the ground as a proof of concept. Future work should explore the sensitivity of existing ground-based measurements of the ionosphere and assess the feasibility of this proof of concept study given our predictions for soliton characteristics.

Finally, a systems architecture trade should be completed. We have designed a 2U CubeSat using commercial components that could detect precursor solitons. However, in completing this design, the advantages of a larger vehicle (perhaps 6U) became clear. Specifically, one of the major weakness of the 2U platform is that the electric potential of the CubeSat may vary, necessitating the floating potential probe. Future work should investigate whether a 6U vehicle is large enough to have a fixed electric potential. Additionally, a 6U CubeSat would remove the need for deployable solar panels and provide the volume necessary for a propulsion system, which is needed for end of life disposal from altitudes above 900km. Additionally, a propulsion system would enable a single fleet of CubeSats to change their semi-major axis in order to map the debris in more than one 100km altitude ring. A final trade to be considered is whether this instrument is best suited to be a hosted payload on a full-sized LEO vehicle. As mentioned previously, the Langmuir probe itself poses few mass, volume, power or data rate constraints on a host vehicle. The main constraint of the Langmuir probe is that it must not be in the spacecraft's plasma sheath or plasma wake. Having a small (2U) vehicle actually increases the complexity of the mission due to the variation in the electric potential of the CubeSat. Thus, future work should evaluate whether or not the attitude requirements of the Langmuir probe eliminate the feasibility of using this instrument as a hosted payload.

References

[1] Christiansen, E., Hyde, J., and Bernhard, R., "Space Shuttle Debris and Meteoroid Impacts," Advances in Space Research, Vol. 34, No. 5, 2004, pp. 1097–1103.

[2] Sen, A., Tiwari, S., Mishra, S., and Kaw, P., "Nonlinear Wave Excitations by Orbiting Charged Space Debris Objects," Advances in Space Research, Vol. 56, 2015, pp. 429–435.

[3] Jaiswal, S., Bandyopadhyay, P., and Sen, A., "Experimental Observation of Precursor Solitons in a Flowing Complex Plasma," Physical Review E, Vol. 93, 2016, pp. 041201.

[4] Tiwari, S. and Sen, A., "Wakes and Precursor Soliton Excitations by a Moving Charged Object in a Plasma," Physics of Plasmas, Vol. 23, 2016, pp. 022301.

[5] Available at `https://orbitaldebris.jsc.nasa.gov/faq.html#3`, December 2018.

[6] Council, N. R., Orbital Debris: A Technical Assessment, National Academies Press, Jun 1995.

[7] NASA, NASA Technology Roadmaps: TA 5: Communications, Navigation and Orbital Debris Tracking and Characterization Systems, chap. 5.7 Orbital Debris Tracking and Characterization, NASA, 2015.

[8] Liou, J.-C., Matney, M. J., Anz-Meador, P. D., Kessler, D., Jansen, M., and Theall, J. R., "The New NASA Orbital Debris Engineering Model ORDEM2000," Tech. rep., NASA, 2002.

[9] "Soliton Wave Receives Crowd of Admirers," Nature, Vol. 376, August 1995, pp. 373.

[10] Li, X., Dong, C., Clemente-Colón, P., Pichel, W. G., and Friedman, K. S., "Synthetic Aperature Radar Observation of the Sea Surface Imprints of Upstream Atmospheric Solitons Generated by Flow Impeded by an Island," Journal of Geophysical Research, Vol. 109, 2004, pp. C02016.

[11] Trines, R., Bingham, R., Dunlop, M. W., Vaivads, A., Davies, J. A., Mendonça, J. T., Silva, L. O., and Shukla, P. K., "Spontaneous Generation of Self-Organized Solitary Wave Structures at Earth's Magnetopause," Physical Review Letters, Vol. 99, No. 20, Nov 2007.

[12] Fish, C., Swenson, C., Crowley, G., et al., "Design, Development, Implementation and On-orbit Performance of the Dynamic Ionosphere CubeSat Experiment Mission," Space Science Reviews, Vol. 181, 2014, pp. 61–120.

[13] Goree, J., "Charging of particles in a plasma," Plasma Sources Science and Technology, Vol. 3, No. 3, Aug 1994, pp. 400–406.

[14] Sodha, M. S. and Mishra, S. K., "Modification of electron density in F layer of ionosphere by dust suspension," Physics of Plasmas, Vol. 24, No. 4, Apr 2017, pp. 43705.

[15] Prol, F. d. S., Hernandez-Pajares, M., Camargo, P. d. O., and Muella, M. T. d. A. H., "Spatial and Temporal Features of the Topside Ionospheric Electron Density by a New Model Based On GPS Radio Occultation Data," Journal of Geophysical Research: Space Physics, Mar 2018.

[16] Sibanda, P. and McKinnell, L. A., "Topside ionospheric vertical electron density profile reconstruction using GPS and ionosonde data: possibilities for South Africa," Annales Geophysicae, Vol. 29, No. 2, Feb 2011, pp. 229–236.

[17] Marinov, P., Kutiev, I., Belehaki, A., and Tsagouri, I., "Modeling the plasmasphere to topside ionosphere scale height ratio," Journal of Space Weather and Space Climate, Vol. 5, 2015, pp. A27.

[18] Hastings, D. E., "A review of plasma interactions with spacecraft in low Earth orbit," Journal of Geophysical Research, Vol. 100, No. A8, 1995, pp. 144–157.

[19] Denton, M. H., "Bulk plasma properties at geosynchronous orbit," Journal of Geophysical Research, Vol. 110, No. A7, 2005.

[20] Nishida, A., "Average structure and storm-time change of the polar topside ionosphere at sunspot minimum," Journal of Geophysical Research, Vol. 72, No. 23, Dec 1967, pp. 6051–6061.

[21] Leach, R., Alexander, M., Analysis, S., Electromagnetics, I. L. G. C. M. S. F. C., and Branch, E., Failures and anomalies attributed to spacecraft charging, NASA reference publication, National Aeronautics and Space Administration, Marshall Space Flight Center, 1995.

[22] Tay, K. G., "Method of Lines and Pseudospectral Solutions of the Forced Korteweg-de Vries Equation with Variable Coefficients Arises in Elastic Tube," International Journal of Pure and Applied Mathematics, Vol. 116, Nov 2017, pp. 985–998.

[23] Lindqvist, P. A., Marklund, G. T., and Blomberg, L. G., "Plasma characteristics determined by the Freja electric field instrument," Space Science Reviews, Vol. 70, No. 3–4, Nov 1994, pp. 593–602.

[24] Shi, J., Xu, B., Torkar, K., Zhang, T., and Liu, Z., "An electrostatic model for nonlinear waves in the upper ionosphere," Advances in Space Research, Vol. 32, No. 3, Jan 2003, pp. 303–308.

[25] Widner, M., "Plasma Expansion into a Vacuum," Physics of Fluids, Vol. 14, No. 4, 1971, pp. 795.

[26] Alpers, W., Wang-Chen, H., and Hock, L., "Observation of internal waves in the Andaman Sea by ERS SAR," IGARSS'97. 1997 IEEE International Geoscience and Remote Sensing Symposium Proceedings. Remote Sensing - A Scientific Vision for Sustainable Development, IEEE, 1997, pp. 1287–1292.

[27] Mitnik, L. and Dubina, V., "Spatial-temporal distribution and characteristics of internal waves in the Okhotsk and Japan Seas studied by ERS-1/2 SAR and Envisat ASAR," European Space Agency, (Special Publication) ESA SP, 07 2007.

[28] Russell, J., "Report of the fourteenth meeting of the British Association for the Advancement of Science, York," 1844.

[29] Korteweg, D. J. and de Vries, G., "XLI. On the change of form of long waves advancing in a rectangular canal, and on a new type of long stationary waves," The London, Edinburgh, and Dublin Philosophical Magazine and Journal of Science, Vol. 39, No. 240, May 1895, pp. 422–443.

[30] Washimi, H. and Taniuti, T., "Propagation of Ion-Acoustic Solitary Waves of Small Amplitude," Physical Review Letters, Vol. 17, No. 19, Nov 1966, pp. 996–998.

[31] Shen, S. S., A Course on Nonlinear Waves, Springer Netherlands, 1993.

[32] Wu, T. Y.-T., "Generation of upstream advancing solitons by moving disturbances," Journal of Fluid Mechanics, Vol. 184, No. 1, Nov 1987, pp. 75.

[33] Nouri Kadijani, M. and Zaremoghaddam, H., "Effect of Dust Grains on Dust-Ion-Acoustic KdV Solitons in Magnetized Complex Plasma with Superthermal Electrons," Journal of Fusion Energy, Vol. 31, No. 5, Nov 2011, pp. 455–462.

[34] Sultana, S., "Ion acoustic solitons in magnetized collisional non-thermal dusty plasmas," Physics Letters A, Vol. 382, No. 20, May 2018, pp. 1368–1373.

[35] Cabral, M. and Rosa, R., "Chaos for a damped and forced KdV equation," Physica D: Nonlinear Phenomena, Vol. 192, No. 3–4, Jun 2004, pp. 265–278.

[36] Ott, E., "Damping of Solitary Waves," Physics of Fluids, Vol. 13, No. 6, 1970, pp. 1432.

[37] Pierrard, V. and Lemaire, J., "Lorentzian ion exosphere model," Journal of Geophysical Research: Space Physics, Vol. 101, No. A4, Apr 1996, pp. 7923–7934.

[38] Livadiotis, G., "Statistical origin and properties of kappa distributions," Journal of Physics: Conference Series, Vol. 900, Sep 2017, pp. 12014.

[39] Pierrard, V. and Stegen, K., "A three-dimensional dynamic kinetic model of the plasmasphere," Journal of Geophysical Research: Space Physics, Vol. 113, No. A10, Oct 2008.

[40] Pierrard, V. and Lazar, M., "Kappa Distributions: Theory and Applications in Space Plasmas," Solar Physics, Vol. 267, No. 1, Oct 2010, pp. 153–174.

[41] Lemaire, J. and Scherer, M., "Exospheric models of the topside ionosphere," Space Science Reviews, Vol. 15, No. 5, Mar 1974.

[42] Prölss, G. W. and Bird, M. K., Physics of the Earth's Space Environment: an introduction, Springer-Verlag Berlin Heidelberg, 2004.

[43] De Bibhas, R., "Electric potential on solid spheres in a plasma," Astrophysics and Space Science, Vol. 30, No. 1, Sep 1974, pp. 135–147.

[44] Goebel, D. M. and Katz, I., Fundamentals of Electric Propulsion, John Wiley & Sons, Inc., Jul 2008.

[45] Grimshaw, R., Maleewong, M., and Asavanant, J., "Stability of gravity-capillary waves generated by a moving pressure disturbance in water of finite depth," Physics of Fluids, Vol. 21, No. 8, Aug 2009, pp. 82–101.

[46] Fornberg, B. and Whitham, G. B., "A Numerical and Theoretical Study of Certain Nonlinear Wave Phenomena," Philosophical Transactions of the Royal Society A: Mathematical, Physical and Engineering Sciences, Vol. 289, No. 1361, May 1978, pp. 373–404.

[47] Chan, T. F. and Kerkhoven, T., "Fourier Methods with Extended Stability Intervals for the Korteweg-De Vries Equation," SIAM Journal on Numerical Analysis, Vol. 22, No. 3, 1985, pp. 441–454.

[48] Jun-Xiao, Z. and Bo-Ling, G., "Analytic Solutions to Forced KdV Equation," Communications in Theoretical Physics, Vol. 52, No. 2, Aug 2009, pp. 279–283.

[49] Nouri, F. and Sloan, D., "A comparison of fourier pseudospectral methods for the solution of the Korteweg-de Vries equation," Journal of Computational Physics, Vol. 83, No. 2, Aug 1989, pp. 324–344.

[50] Wadati, M. and Toda, M., "The Exact N-Soliton Solution of the Korteweg-de Vries Equation," Journal of the Physical Society of Japan, Vol. 32, No. 5, May 1972, pp. 1403–1411.

[51] Grimshaw, R., Pelinovsky, E., and Tian, X., "Interaction of a solitary wave with an external force," Physica D: Nonlinear Phenomena, Vol. 77, No. 4, Oct 1994, pp. 405–433.

[52] Chang, C.-H. and Wang, K.-H., "Generation of Three-Dimensional Fully Nonlinear Water Waves by a Submerged Moving Object," Journal of Engineering Mechanics, Vol. 137, No. 2, Feb 2011, pp. 101–112.

[53] Katsis, C. and Akylas, T. R., "On the excitation of long nonlinear water waves by a moving pressure distribution. Part 2. Three-dimensional effects," Journal of Fluid Mechanics, Vol. 177, No. 1, Apr 1987, pp. 49.

[54] Moroz, I. M., "The Kadomtsev–Petviashvili equation under rapid forcing," Journal of Mathematical Physics, Vol. 38, No. 6, Jun 1997, pp. 3110–3122.

[55] Petviashvili, V. and Pokhotelov, O., Solitary waves in plasmas and in the atmosphere., 1992.

[56] Seadawy, A. and El-Rashidy, K., "Dispersive solitary wave solutions of Kadomtsev-Petviashvili and modified Kadomtsev-Petviashvili dynamical equations in unmagnetized dust plasma," Results in Physics, Vol. 8, Mar 2018, pp. 1216–1222.

[57] ANNOU, K., BAHAMIDA, S., and ANNOU, R., "Spherical Kadomtsev–Petviashvili equation for dust acoustic waves with dust size distribution and two-charges-ions," Pramana, Vol. 76, No. 3, Mar 2011, pp. 513–518.

[58] "Long Duration Exposure Facility Website," Available at https://curator.jsc.nasa.gov/mic/ldef/index.cfm.

[59] Ranvier, S., Anciaux, M., Cardoen, P., Gamby, E., Bonnewijn, I. S., De Keyser, J., Pieroux, D., and Lebreton, J., "Use of a Langmuir Probe Instrument on Board a Pico-Satellite," IEEE Transactions on Plasma Science, Vol. 45, No. 8, 2017, pp. 2007–2012.

[60] Hoang, H., Røed, K., Bekkeng, T. A., Moen, J. I., Clausen, L. B. N., Trondsen, E., Lybekk, B., Strøm, H., Bang-Hauge, D. M., Pedersen, A., Nokes, C. D. A., Cupido, C., Mann, I. R., Ariel, M., Portnoy, D., and Sagi, E., "The Multi-needle Langmuir Probe Instrument for QB50 Mission: Case Studies of Ex-Alta 1 and Hoopoe Satellites," Space Science Reviews, Vol. 215, No. 2, Feb 2019, pp. 21.

[61] "Cadet UHF and UHF Plus S-Band Radios," Available at https://www.sdl.usu.edu/downloads/cadet-radios.pdf, 2012.

[62] Sakovsky, M., Pellegrino, S., and Costantine, J., "Rapid design of deployable antennas for CubeSats," IEEE Antennas and Propagation Magazine, April, 2017, pp. 50–58.

[63] "Dipole antenna system," Available at https://www.isispace.nl/product/dipole-antenna/.

[64] Mehrparvar, A., Pignatelli, D., Carnahan, J., Munakat, R., Lan, W., Toorian, A., Hutputanasin, A., and Lee, S., "Cubesat design specification rev. 13," The CubeSat Program, Cal Poly San Luis Obispo, US, Vol. 1, 2014, pp. 2.

[65] "ISIS On Board Computer," Available at https://www.cubesatshop.com/wp-content/uploads/2016/06/iOBC-Brochure-v1.pdf.

[66] "ISIS antenna systems brochure," Available at https://www.cubesatshop.com/wp-content/uploads/2016/06/ISIS-Antenna-systems-Brochure-v1.pdf.

[67] "Maryland Aerospace: IR-EHS CubeSat ADACS," Available at http://www.adcolemai.com/wp-content/uploads/2019/02/AMA-MAI-400-Datasheet.pdf.

[68] "Maryland Aerospace: CubeSat Sun Sensors," Available at http://www.adcolemai.com/wp-content/uploads/2019/02/AMA-MAI-Sun-Sensor.pdf.

[69] Clark, C. and Logan, R., "Power budgets for mission success," Clyde Space, 2011.

[70] "Crystalspace P1U "Vasik"," Available at https://www.cubesatshop.com/product/crystalspace-p1u-vasik/.

[71] "CubeSat Solar panel DHV-CS-10," Available at https://www.cubesatshop.com/product/cubesat-solar-panels/.

[72] Escobar, A. C., A langmuir probe instrument for research in the terrestrial ionosphere, Master's thesis, State College, Pennsylvania, 2009.

[73] "2-Unit cubesat structure," Available at https://www.cubesatshop.com/product/2-unit-cubesat-structure/.

[74] Albarran, R. M. and Barjatya, A., "Plasma Density Analysis of CubeSat Wakes in the Earth's Ionosphere," Journal of Spacecraft and Rockets, 2016, pp. 393–400.

[75] Committee, I.-A. D. C., "IADC Space Debris Mitigation Guidelines," Tech. Rep. IADC-02-01, https://www.iadc-online.org/Documents/, 2007.

[76] Meyer, K. and Chao, C., "Atmospheric Reentry Disposal for Low-Altitude Spacecraft," Journal of Spacecraft and Rockets, Vol. 37, No. 5, 2000, pp. 670–674.

[77] Fuller, J. K., Hinkley, D., and Janson, S. W., "CubeSat Balloon Drag Devices: Meeting the 25-Year De-Orbit Requirement," 2010.

[78] Tsay, M. et al., "Complete EM System Development for Busek's 1U CubeSat Green Propulsion Module," 52nd AIAA/SAE/ASEE Joint Propulsion Conference, 2016.

[79] Carpenter, C. B. et al., "CubeSat modular propulsion systems product line development status and mission applications," 49th AIAA/ASME/SAE/ASEE Joint Propulsion Conference, 2013.

[80] Hastings, D. and Garrett, H., Spacecraft-environment interactions, Cambridge university press, 2004.

[81] Hoang, H., Røed, K., Bekkeng, T., Trondsen, E., Clausen, L., Miloch, W., and Moen, J., "High-spatial-resolution electron density measurement by Langmuir probe for multi-point observations using tiny spacecraft," Measurement Science and Technology, Vol. 28, No. 11, 2017, pp. 115903.

[82] Holtgreven, W. L., "Plasma Diagnostics," 1968.

[83] Brace, L. H., "Langmuir probe measurements in the ionosphere," Geophysical Monograph-American Geophysical Union, Vol. 102, 1998, pp. 23–36.

[84] Hoegy, W. and Wharton, L. E., "Current to a moving cylindrical electrostatic probe," Journal of Applied Physics, Vol. 44, No. 12, 1973, pp. 5365–5371.

[85] Suresh, P., Surface morphology implications on Langmuir probe measurements, Master's thesis, Logan, Utah, 2011.

[86] Auman, A. J., The Adaptability of Langmuir Probes to the Pico-Satellite Regime, Ph.D. thesis, Logan, Utah, 2008.

[87] Na, G. W., Yang, J., Ryu, K., Lee, J. C., and Min, K. W., "Test of Langmuir probes developed for the CubeSat LINK," Journal of the Korean Physical Society, Vol. 68, No. 3, 2016, pp. 482–485.

[88] Abe, T., Oyama, K.-i., et al., An Introduction to Space Instrumentation, chap. Langmuir probe, Terrapub, 2013, pp. 63–75.

[89] Gulyaeva, T. and Titheridge, J., "Advanced specification of electron density and temperature in the IRI ionosphere–plasmasphere model," Advances in Space Research, Vol. 38, No. 11, 2006, pp. 2587–2595.

[90] Norton, R. and Findlay, J., "Electron density and temperature in the vicinity of the 29 September 1967 middle latitude red arc," Planetary and Space Science, Vol. 17, No. 11, 1969, pp. 1867–1877.

[91] Gregory, J. D., Design, test, and calibration of the Utah State University floating potential probe, Master's thesis, 2009.

[92] Barjatya, A., Swenson, C. M., Thompson, D. C., and Wright Jr, K. H., "Data analysis of the floating potential measurement unit aboard the international space station," Review of Scientific Instruments, Vol. 80, No. 4, 2009, pp. 041301.

[93] Chen, X. and Sánchez-Arriaga, G., "Current-Voltage and Floating-Potential characteristics of cylindrical emissive probes from a full-kinetic model based on the orbital motion theory," Journal of Physics: Conference Series, Vol. 958, IOP Publishing, 2018, p. 012001.

[94] Parker, L. W., "Calculation of sheath and wake structure about a pillbox-shaped spacecraft in a flowing plasma," 1977.

[95] Giono, G., Maxouffre, S., Theroude, C., Popelier, L., Loubere, D., Dannenmayer, K., Gudmundsson, J. T., Ivchenko, N., Olentsenko, G., and Merino, M., "Experimental Determination of the Plasma Properties in the Far-plume of an SPT-100 Hall Thruster," 35th International Electric Propulsion Conference, Georgia Institute of Technology, Vol. 35, 2017.

[96] Biersteker, S., A Nanosatellite Mission for Ionospheric Disturbance Monitoring: Mission Design and Payload Description, Master's thesis, 2016.

[97] Olson, J., Brenning, N., Wahlund, J.-E., and Gunell, H., "On the interpretation of Langmuir probe data inside a spacecraft sheath," Review of Scientific Instruments, Vol. 81, No. 10, 2010, pp. 105106.

[98] Szuszczewicz, E. P., "Area influences and floating potentials in Langmuir probe measurements," Journal of Applied Physics, Vol. 43, No. 3, 1972, pp. 874–880.

[99] Amatucci, W., Koepke, M., Sheridan, T., Alport, M., and Carroll III, J., "Self-cleaning Langmuir probe," Review of scientific instruments, Vol. 64, No. 5, 1993, pp. 1253–1256.

[100] International, L. D., "Digisonde Portable Sounder Technical Manual," Available at `http://digisonde.com/pdfs/Digisonde4DManual_LDI-web1-2-6.pdf`.

[101] Zhang, S.-R., Rukao, S., Oliver, W. L., and Otsuka, Y., "The Height of the Maximum Ionospheric Electron Density over the MU Radar," Journal of Atmospheric and Solar-Terrestrial Physics, Vol. 61, 1999, pp. 1367–1383.

[102] Hoang, H., Roed, K., Bekkeng, T., Moen, J., et al., "The Multi-Needle Langmuir Probe Instrument for QB50 Mission: Case Studies of Ex-Alta 1 and Hoopoe Satellites," Space Science Reviews, Vol. 215, 2019, pp. 21.